An enhanced three-dimensional reduced-order track model for predicting differential settlement in railway transition zones on stratified soils

Transportation Geotechnics 61 (2026) 102040

Contents lists available at ScienceDirect

Transportation Geotechnics

journal homepage: www.elsevier.com/locate/trgeo

Original article

An enhanced three-dimensional reduced-order track model for predicting differential settlement in railway transition zones on stratified soils

Kourosh Nasrollahi [a,*], Jens C.O. Nielsen [b], Jelke Dijkstra [c]

[a] Department of Architecture and Civil Engineering, Division of Structural Engineering, Chalmers University of Technology, SE-412 96 Gothenburg, Sweden
[b] Department of Mechanical Engineering, Division of Dynamics/CHARMEC, Chalmers University of Technology, SE-412 96 Gothenburg, Sweden
[c] Department of Architecture and Civil Engineering, Division of Geology and Geotechnics, Chalmers University of Technology, SE-412 96 Gothenburg, Sweden

ARTICLE INFO

Keywords:
Transition zone
Differential settlement
Dynamic vehicle–track interaction
Flexible sleeper
Reduced-order model
Mitigation measures

ABSTRACT

Railway transition zones between two distinct track forms are prone to differential settlement, which can undermine track performance and increase maintenance demands over time. Accurately predicting the long-term evolution of settlement in these zones remains challenging due to the complex interplay between dynamic vehicle–track interaction, changing support conditions, and the gradual development of track geometry irregularities. This study presents a methodology for simulating long-term differential track settlement in railway transition zones using time-domain analyses of vertical dynamic vehicle–track interaction. The approach accounts for the formation of voided sleepers, the redistribution of sleeper–ballast contact pressure across the transition zone, and the progressive evolution of vertical track irregularities. The computational framework integrates a two-dimensional (2D) vehicle model, a three-dimensional (3D) non-linear finite element (FE) model of the track superstructure, and a linear 3D FE model of the layered subgrade. Mitigation measures installed within the substructure to alleviate stiffness gradients between track forms are also represented. Rails and sleepers are modelled using Euler–Bernoulli beam finite elements. To enhance computational efficiency, the subgrade model is reduced via static condensation to form a reduced-order model (ROM). The methodology is applied to transition zones between ballasted track on embankment and slab track on a bridge or in a tunnel. In each iteration step, a short-term dynamic analysis determines the contact pressure distribution at each sleeper–ballast interface, providing the basis for calculating ballast settlement increments. Simultaneously, the depth-dependent deviatoric stress distribution is evaluated to estimate permanent deformation within the subgrade layers. Iterations proceed until the specified cumulative traffic load is reached, enabling prediction of long-term settlement development. The results show that differential settlement develops predominantly on the ballasted side of the transition, with a local maximum occurring between sleepers 5 and 10 from the transition. The precise location of the maximum depends on traffic direction. For traffic moving from softer ballasted track towards stiffer slab track, the maximum occurs at sleeper 8, whereas the reverse direction produces a maximum at sleeper 5, with slightly larger magnitude in the former case. Over time, settlement accumulation stabilises due to hardening behaviour in the settlement models. The proposed framework provides a robust basis for evaluating the long-term performance of railway transition zones and for assessing the effectiveness of substructure mitigation measures.

Introduction

In a railway transition zone between two distinct track forms, differences in superstructure and/or substructure design create a spatial variation in track stiffness. Typical examples include transitions from slab track to ballasted track and from an embankment to a bridge or tunnel [1–12]. Variations in the resulting dynamic loading and support conditions on either side of the transition often lead to differential settlement of ballast and subgrade, voided sleepers, and irregularities in the longitudinal track level shortly after construction. These effects intensify the dynamic traffic loading across the transition zone, accelerating the deterioration of the ballast and subgrade layers [5].

The primary objective of transition zone design is to minimise the track stiffness gradient at rail level between the open track and the adjacent structure [3,6,13]. Achieving a more uniform vertical

* Correspondence to: Department of Architecture and Civil Engineering, Division of Structural Engineering, Chalmers University of Technology, SE-412 96, Gothenburg, Sweden.
E-mail address: kourosh.nasrollahi@chalmers.se (K. Nasrollahi).

https://doi.org/10.1016/j.trgeo.2026.102040
Received 30 January 2026; Received in revised form 9 April 2026; Accepted 11 April 2026
Available online 22 April 2026

stiffness along the track ensures a more homogeneous distribution of stresses within the supporting layers, thereby reducing localised stress concentrations and mitigating differential settlement. These variations in stiffness are primarily attributed to spatial variability in the geotechnical conditions, as identified in the site investigation (e.g. changes in soil stratigraphy, strength and stiffness parameters, and groundwater conditions). Mitigation measures can be categorised in terms of their location: in the substructure, in the superstructure, or in both. These solutions can be divided into four distinct groupings [13]: (1) mitigation of stiffness gradient; (2) enhancement of track foundation; (3) minimisation of differential permanent displacements; and (4) combined superstructure–substructure methodologies [14]. Typical transition zone lengths range from 5 to 30 metres. Guidelines recommend a length equivalent to the distance a vehicle (at maximum line speed) travels in half a second, see [3,4,13]. A list of different transition-zone design concepts is provided in [15]

The ballast layer exhibits highly non-linear deformation under load, with potential voids evolving between the sleeper and ballast. Energy is dissipated into the subgrade strata both through interparticle friction and radiation damping [16]. To represent the ballast and subgrade layers and their interaction with the superstructure, several analyses have been conducted using a two-parameter linear model for each sleeper support, see e.g. [5]. An extended version of this model introduces ballast masses connected by shear springs and dashpots, allowing for the interaction between adjacent sleepers through the ballast [6]. A review of such models can be found in [16].

Various 3D models have been applied to capture the full complexity of the dynamics of a railway track on layered soil. In [17], a study was conducted on finite element time-domain modelling of moving loads on railway tracks supported by an elastic soil domain. The investigation compared various mesh geometries, boundary conditions, and damping models for the subgrade. Although reflections from the boundaries were not completely eliminated, the approach achieved a practically sufficient level of suppression using a cuboid mesh with fixed boundaries and mass-proportional damping. The required volume of the model to suppress spurious vibrations was evaluated, revealing that significant extensions of the model were required near critical speeds in homogeneous half-spaces. Furthermore, incorporation of advanced boundary conditions, such as perfectly matched layers to reduce the size of the model, has been demonstrated to improve the efficiency of simulations of dynamic vehicle–track interaction [6,18]. However, the computational time remains high.

An attractive approach, adopted herein, is to integrate a ROM of the 3D layered subgrade with a simpler superstructure model to reduce the computational cost [19]. These techniques are particularly effective for linear problems, where superposition holds and the reduced basis can capture the system response accurately with minimal loss of fidelity. Examples of techniques for reduced-order modelling include component mode synthesis (CMS), static condensation, proper orthogonal decomposition (POD), and the Craig–Bampton method [20,21]. Vilhelmson et al. [22] employed Craig–Bampton model reduction to condense the FE representations of the rail and sleeper bodies into corresponding substructures for multi-body simulation of vehicle–track interaction in a crossing panel, extending an earlier beam-based track model by introducing a 3D solid FE representation of the crossing rail to better capture local structural loading and calibrating key support-condition parameters against field measurements from an instrumented turnout demonstrator.

A benchmark study comparing the performance of a 2D model (developed by our research group) and a 3D model (from another research group) for predicting long-term settlement in a transition zone was presented in [6]. In the 2D model, the foundation was represented by seven parameters, including a rigid mass for the ballast under each sleeper, and discrete springs and dampers representing the stiffness and damping of the ballast and subgrade. In [6], the full 3D finite element model, including an extensive representation of the subgrade and foundation, required approximately 48 h of CPU time to perform a single simulation of short-term dynamic vehicle–track interaction, whereas the corresponding 2D model required only 2–3 h. This substantial reduction in computational effort provides strong motivation for implementing a ROM for the layered subgrade in the present work.

In the current study, the substructure, including the layered soil and any construction measures aimed at reducing the stiffness gradient in the transition zone (e.g., a transition wedge), is first modelled in full detail using a 3D linear finite element model. The subsequent step involves static condensation to compute a stiffness matrix representing only a small number of retained DOFs of the substructure at the interfaces with the superstructure. This ROM is then assembled with a 3D nonlinear model of the superstructure, including beam elements for the flexible sleepers. The decision to apply static condensation for the subgrade is motivated by the findings of the dynamic finite element analyses conducted by Grabe [23], which showed that, for train speeds of up to 240 km/h, dynamic effects have a relatively minor influence on the calculated maximum stress variations in the ground beneath a railway line. Furthermore, for speeds below 140 km/h, the ground response to moving train loads can be considered to be essentially quasi-static [24]. Nevertheless, in a coupled vehicle–track–soil system, the significance of the induced dynamic effects depends on the dynamic stiffness, damping, and layering of the supporting ground, as well as on the relationship between train speed, characteristic wave propagation velocities (or effective critical velocity), and the excitation frequencies associated with axle, bogie, and car body passings. Therefore, for soft ground conditions, significant dynamic amplification may occur even at lower train speeds.

A wide range of empirical models have been developed to predict the accumulation of plastic strain in coarse-grained materials under cyclic loading, drawing on extensive laboratory testing and field monitoring data. These models generally incorporate critical factors such as the mean (effective) stress in the material, the component of deviatoric stress arising from cyclic loading, and the number of load cycles, in order to formulate a hardening law that captures the evolution of (incremental) subgrade stiffness, and the accumulation of permanent deformation. All of these aspects are essential for evaluating the long-term behaviour of track–substructure systems under repeated train loading [25–28]. The development of differential settlement leads to increasing dynamic loading, which in turn leads to accelerated rates of settlement in the ballast and subgrade materials. The stress amplitude in the strain accumulation models [29] needs to be updated based on the accumulated strain in the system, to capture this intricate soil-structure-interaction mechanism where stress and strain evolve as vehicles pass over the transition.

Several studies have integrated empirical settlement models into train–track dynamic interaction frameworks to predict settlement, accounting for dynamic wheel–rail contact forces that induce time-varying stress in the subgrade. Simplified 2D models combined with empirical settlement formulae offer computational efficiency but require calibration and extrapolation to predict long-term settlement [5,6]. Existing mechanistic–empirical settlement formulae are reviewed in [30].

This study presents a computationally efficient numerical simulation framework for predicting long-term differential settlement in railway transition zones between ballasted and slab track systems. Although the iterative settlement formulation and certain elements of the vehicle–track interaction model build on the authors' earlier work, the principal novel contribution lies in the incorporation of a reduced-order representation of a 3D multilayered subgrade within the settlement analysis of the coupled vehicle–track–subgrade system. This development enables long-term simulations over millions of wheel passages while retaining the essential mechanical influence of subgrade stratification and of any mitigation measures implemented within the substructure to enhance support conditions, including their effects on stiffness variation along the track and the resulting settlement behaviour. Another novel contribution of the proposed framework is its

ability to distinguish between permanent deformations occurring in the ballast and those occurring in the subgrade. This capability is important for understanding the governing mechanisms in transition zones and for selecting appropriate mitigation strategies. In contrast to simplified spring–damper representations of the subgrade, the present approach preserves a more realistic description of layered soil behaviour while remaining computationally feasible for iterative dynamic analyses. The framework also provides a consistent simulation environment for evaluating and comparing mitigation measures in transition zones, such as transition wedges and approach slabs, and for assessing their performance under different directions of vehicle travel. Future work will focus on further validation against additional field data, extension to a broader range of transition zone designs and soil conditions, and investigation of uncertainty and parameter sensitivity in long-term settlement predictions.

Simulation framework

The simulation framework uses an iterative approach with a time-domain model of short-term vertical vehicle–track dynamic interaction, accounting for voided sleepers and state-dependent support properties at each sleeper–ballast node interface. In practical railway engineering, it is commonly accepted to distinguish between the resilient response to a single train passage (short-term behaviour) and the permanent accumulation of settlement over numerous cycles (long-term behaviour). Under typical service loads, the subgrade response during an individual passage is predominantly elastic and can therefore be reasonably represented by a linear elastic model. This approach is consistent with established mechanistic–empirical methodologies, in which the transient stress field is obtained from a linear elastic analysis and the long-term settlement is subsequently evaluated through empirical relationships. In addition, implementing a nonlinear constitutive model within a full-scale FE track model would significantly increase the computational cost, particularly when repeated loading over many cycles is required. For this reason, the FE model is used here to capture the short-term response during each train passage, while long-term settlement is incorporated through empirical settlement models. This simulation framework, without the 3D model of the subgrade, has previously been validated versus long-term field measurements on the Iron Ore Line [6].

The model is illustrated in Fig. 2 and comprises a 2D vehicle model, a 3D non-linear FE model of the track superstructure, including the transition between a ballasted track form and a stiffer track form on a bridge (or in a tunnel), and a 3D linear FE model of the layered subgrade. The horizontal boundary under the stiffer track form is assumed to be rigid. A ROM with a limited number of retained vertical DOFs is generated by applying static condensation to the linear 3D FE model. This ROM provides the stiffness and damping matrices for the substructure on the ballasted track side. The resulting matrices, containing the components referred to as k_{sub} and c_{sub} in Fig. 2, are assembled with the superstructure model using the DOFs of the ballast masses. This process will be explained in more detail in Section "Track and vehicle models".

The iterative approach is illustrated in the block diagram shown in Fig. 1. In each iteration step, a time-domain simulation of dynamic vehicle–track interaction is performed using pre-calculated static track displacements (due to the gravity load on the track) as initial conditions. Based on the calculated time histories of the forces acting in the spring–damper connections between each sleeper node (each sleeper has five beam elements and six nodes as shown in Fig. 2(b)) and the corresponding ballast mass, the maximum contact pressures at the interfaces between sleepers and ballast (generated by the combination of gravity load and each passing wheel) are identified. These are used to predict the ballast settlement at all the sleepers nodes on the ballasted side [6]. In a post-processing step, the computed sleeper–ballast contact pressure at each sleeper node also serves as input to the Flamant solution [31], enabling the calculation of deviatoric stress at various depths within the subgrade. These stress values are subsequently applied in the Li and Selig model [29] to determine the corresponding strain and permanent displacement of the subgrade layers for each iteration.

After each iteration step, the support conditions (i.e., the vertical positions of the ballast masses) across all sleepers in the ballasted track section of the non-linear track model used in the simulation of the dynamic vehicle–track interaction are updated to reflect the current state. It is assumed that all vehicles within a given iteration step generate the same set of maximum sleeper–ballast contact pressures (here four wheels are considered). This assumption is reasonable when traffic is dominated by a single vehicle type operating within a narrow speed range. This is the case for the Iron Ore Line in northern Sweden, which has been studied extensively throughout this research project. Under such conditions, the signatures of the dynamic track response remain similar between adjacent wagons, see [6,9]. However, if axle loads, speeds, or other operating parameters vary substantially, this assumption becomes less accurate. In such circumstances, different vehicle or loading cases should be treated separately, or a weighted representation of the traffic mix should be adopted. The simulation framework presented here is capable of accommodating such varying operational conditions. By iterating this process, the model predicts the long-term accumulated differential settlement, the potential development of voided sleepers, and the redistribution of foundation loads between adjacent sleepers, as well as along each sleeper.

Track and vehicle models

As illustrated in Fig. 2, the non-linear track model is a FE model featuring rigid boundaries at both ends of the rail. The total length of the track model is 72 metres, consisting of 42 metres of ballasted track and 30 metres of the stiffer track form. The 60E1 rail is undamped and modelled using Euler–Bernoulli beam theory, with four beam elements per sleeper bay. The length of the selected track model and rail discretisation are sufficient to minimise the influence of boundary and discretisation effects on the dynamic response in the transition region [32]. The vehicle and track models are symmetric with respect to a vertical plane centred between the two rails. This assumption is deemed sufficient as the primary objective is to investigate track settlement and the influence of stiffness gradient on the long-term longitudinal track profile (longitudinal level).

A uniform cross-sectional area, A_{sleeper}, is assumed for the concrete sleepers in this study (but this is not a prerequisite of the model). Each half-sleeper is modelled with five beam elements with length 0.25 metres. The sleepers are assumed to be undamped and represented by Euler–Bernoulli beam theory. Consequently, each sleeper has constant bending stiffness, EI_{sleeper}, and mass per unit length, m_{sleeper}, cf [33]. A uniform sleeper spacing of $L = 0.6$ m is considered. The sleeper and rail seat indices for the ballasted track are numbered $i = 1, 2, \ldots, N_{\text{bays}} - 1$ (with $i > 0$), starting from the transition as shown in Fig. 2. Conversely, the stiffer track form is represented as a beam on a rigid engineering structure, with discrete rail support points spaced at 0.6 m intervals. These rail seats are indexed as $i = -1, -2, \ldots$ (with $i < 0$), as also depicted in Fig. 2. Each rail pad is represented by a linear spring–damper element. The ballast layer is modelled using piecewise linear springs and dampers that connect each individual vertical DOF of the sleepers to a corresponding individual ballast mass, see Fig. 2(c). The breakpoint in each bi-linear spring stiffness characteristic corresponds to the voided distance between that sleeper node and its associated ballast mass (in unloaded conditions). The slab is modelled using four Euler–Bernoulli beam elements between each pair of rail seats. The ballast masses represent the vibrating mass of the ballast and are calculated based on formulae in [6,34]. The parameter values for the ballasted and slab track models are summarised in Table 1, while the parameter values for the vehicle model were collected from [5].

In this study, ABAQUS was used to generate a substructure model based on a linear 3D FEM representation of the layered subgrade, from

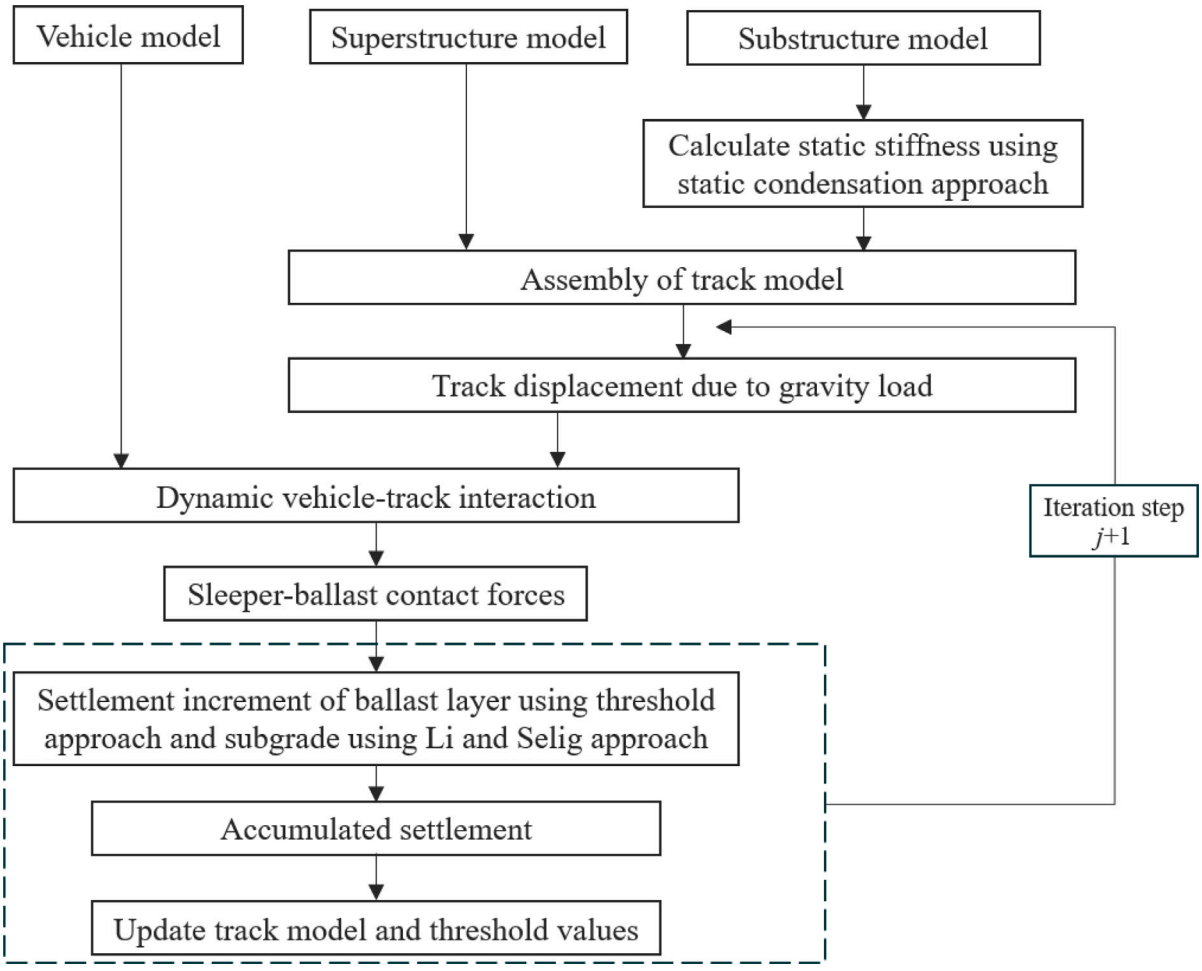

Fig. 1. Iterative procedure to predict differential settlement in a transition zone.

which an equivalent stiffness matrix was derived. This method has the capacity to account for the interaction between multiple foundation points (sleeper nodes across the transition zone). One alternative (used in previous work [5] but not applied in the current study) to determine the equivalent stiffness (non-interacting springs) and damping of a layered subgrade (see k_{sub} and c_{sub} in Fig. 2) is the semi-analytical cone model approach based on one-dimensional wave propagation, as proposed by Wolf and Deeks [35]. Another analytical method is the approach outlined by Gazetas, [36], although this is applicable only to individual sleepers and does not account for the interaction between adjacent sleepers.

The parameterised 3D FE model of the multilayered soil domain was developed to account for the stiffness variation along the ballasted track due to differing support conditions and any implemented measures for mitigating the stiffness gradient (such as a transition wedge). The model (see Fig. 3(a)) is meshed using 8-node brick C3D8R elements. The material behaviour for all layers is assumed to be isotropic and linear elastic, meaning that soil displacements are limited to the elastic range of the stress–strain curve. Regarding the boundary conditions of the domain, symmetry is implemented in the vertical xy-plane (at $z = 0$ m) at the centre of the track between the two rails, by applying a constraint in the z-direction. In the z-direction, the mesh is fixed with a spacing of 0.25 m. Fixed boundary conditions are applied at the bottom and lateral (field side) boundaries of the model. The model domain extends to a depth of 10 m and a width of 10 m. On the upper surface, a uniform element size of 0.2 m in the x-direction is maintained. In contrast, a graded mesh approach is adopted in the lateral (z) and vertical (y) directions, with element sizes gradually increasing from 0.2 m at the upper surface to approximately 1 m at the outer boundaries of the model. In addition, for an application with (reinforced) earthwork, a stiffer material with a length of 20 m along the x-axis at the surface and a slope of 1:1 is introduced, see Fig. 3(b). This region with a horizontal length between 20 m (at the upper surface) and 24 m (at 4 m depth) from the transition was included to capture the influence of a transition wedge on dynamic responses and long-term differential settlement. It is argued that the dynamic response governing ballast (and subgrade) settlement is primarily associated with the pass-by frequencies of axles, bogies, and car bodies, with the car body passing frequency (and higher harmonics) constituting the dominant contribution to the overall frequency content [9]. For the train speeds considered here, this corresponds to excitation frequencies in the range of 1–25 Hz, cf. [9,37]. Within this frequency range, the static representation of the substructure is considered to provide an adequately adequate equivalent stiffness (and damping) for a wide range of subgrade conditions. Since the ROM is constructed using static condensation, the selection of the retained DOFs is based on preserving the essential stiffness and displacement behaviour at each sleeper location, rather than on a dynamic criterion such as a specific frequency range.

The stiffnesses k_{sub} at each coupling between a ballast mass and the corresponding position on the subgrade surface (retained DOFs), see Fig. 2, are assembled in a ROM of the layered subgrade. Static condensation implemented via the **Substructure* generate command in ABAQUS [38] is employed, although it is recognised that this approach does not preserve the full frequency-dependent inertial characteristics of the and linear assumptions are adopted despite the inherently

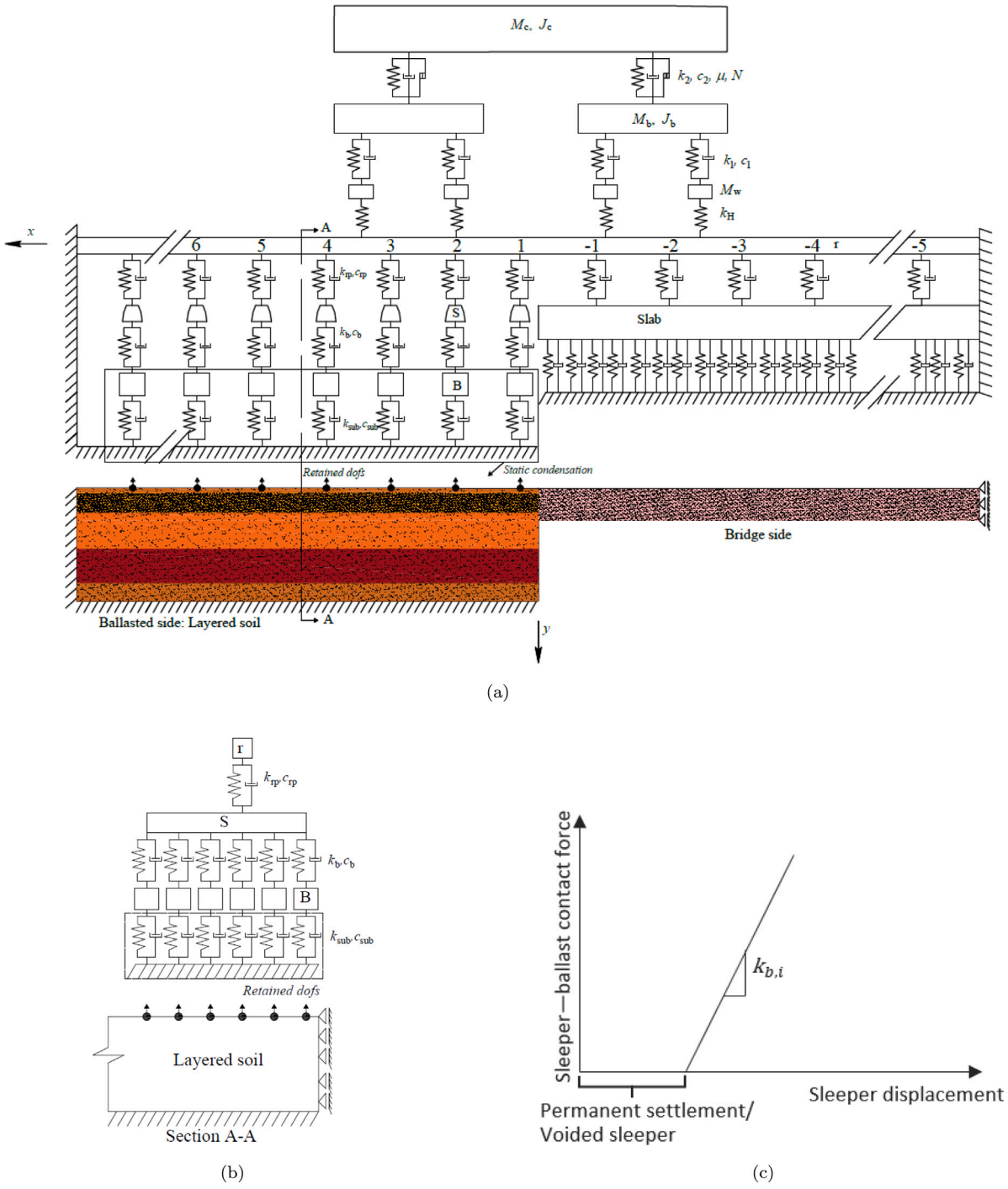

Fig. 2. (a) Sketch of the complete vehicle and transition zone model. (b) Cross-section of the track model, where each half sleeper is represented by five finite element beam elements. (c) Force–displacement characteristics for the spring modelling the ballast stiffness, represented by a piecewise linear relationship.

nonlinear nature of soil behaviour, as deriving a ROM for nonlinear systems remains computationally and theoretically prohibitive in this context. As described above, each sleeper has six vertical DOFs, which are individually coupled to their associated ballast masses.

The DOFs of the linear 3D FE model of the subgrade are partitioned as retained vertical DOFs for all the coupling points (r), while the remaining DOFs are referred to as internal (p) as described by the following equation:

$$\begin{bmatrix}\mathbf{f}_r\\ \mathbf{f}_p\end{bmatrix} = \begin{bmatrix}\mathbf{K}_{rr} & \mathbf{K}_{rp}\\ \mathbf{K}_{pr} & \mathbf{K}_{pp}\end{bmatrix}\begin{bmatrix}\mathbf{r}_r\\ \mathbf{r}_p\end{bmatrix}, \tag{1}$$

where $\mathbf{f}_r$ and $\mathbf{f}_p$ are the external force vectors for the retained and internal DOFs, respectively, $\mathbf{r}_r$ and $\mathbf{r}_p$ are the corresponding displacement vectors, while $\mathbf{K}_{rr}, \mathbf{K}_{rp}, \mathbf{K}_{pr}$ and $\mathbf{K}_{pp}$ are the submatrices of the full stiffness matrix. Since $\mathbf{f}_p = \mathbf{0}$,

$$\mathbf{K}_{pr}\mathbf{r}_r + \mathbf{K}_{pp}\mathbf{r}_p = \mathbf{0} \implies \mathbf{r}_p = -\mathbf{K}_{pp}^{-1}\mathbf{K}_{pr}\,\mathbf{r}_r, \tag{2}$$

Substitution into (1) gives

$$\mathbf{f}_r = \mathbf{K}_{rr}\mathbf{r}_r - \mathbf{K}_{rp}\mathbf{K}_{pp}^{-1}\mathbf{K}_{pr}\,\mathbf{r}_r = \widetilde{\mathbf{K}}_r\,\mathbf{r}_r, \tag{3}$$

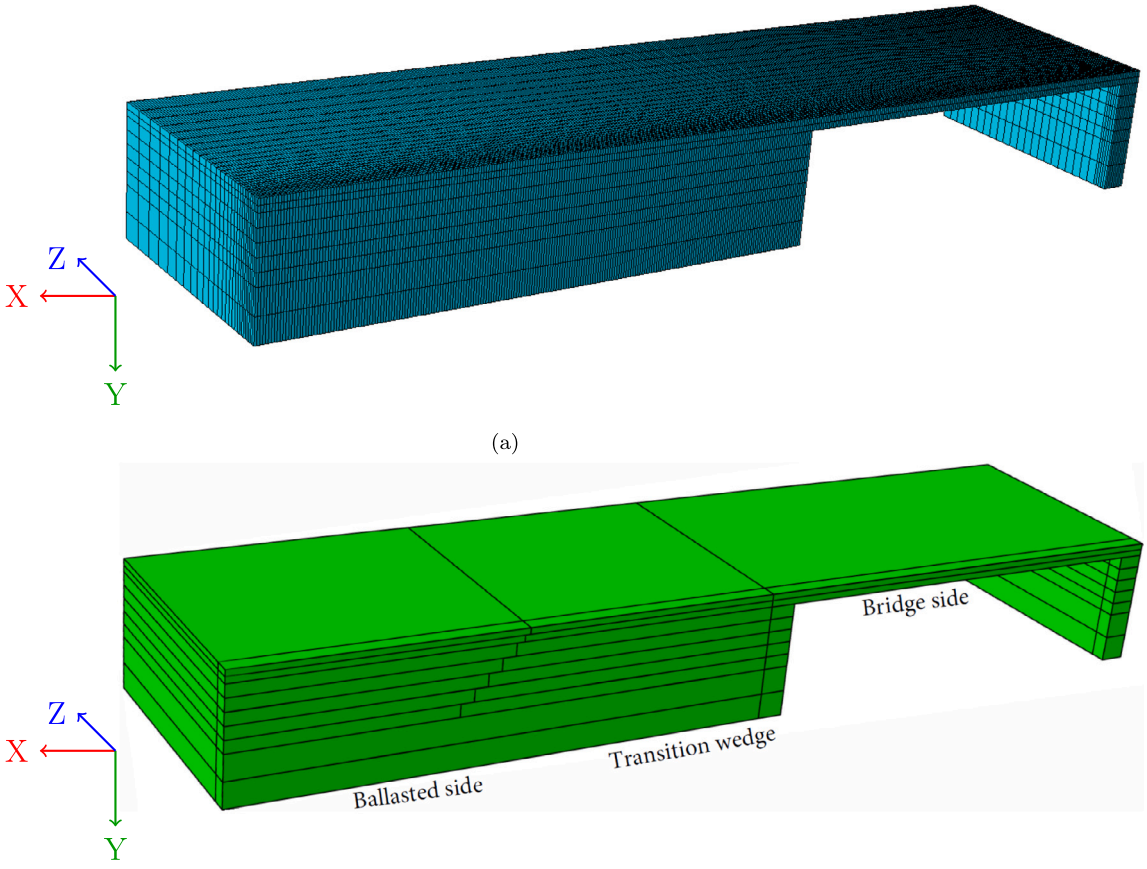

Fig. 3. General 3D FE model of a multilayered subgrade: (a) without a transition wedge (meshed) and (b) with a transition wedge (shown as a staircase shape). The FE model may include layered soil on the ballasted side, as well as a measure to strengthen the support conditions, such as a transition wedge.

Table 1
Parameter values for the track models.

Parameter	Symbol	Value	Unit
Ballasted track on an embankment			
Rail bending stiffness	EI_{rail}	6.4	MN m^2
Rail mass per unit length	m_{rail}	60	kg/m
Rail pad stiffness	k_{rp}	120	MN/m
Rail pad damping	c_{rp}	25	kNs/m
Sleeper bending stiffness	EI_{sleeper}	6.75	MN m^2
Sleeper mass per unit length	m_{sleeper}	120	kg/m
Ballast stiffness per half sleeper	k_{b}	100	MN/m
Ballast damping per half sleeper	c_{b}	25	kNs/m
Ballast mass per half sleeper	m_{b}	400	kg
Subgrade stiffness	k_{sub}	Varying, from ROM	MN/m
Subgrade damping	c_{sub}	Varying, from ROM	kNs/m
Slab track on a rigid engineering structure			
Rail pad stiffness	k_{rp}	120 (stiffer) 60 (softer)	MN/m
Rail pad damping	c_{rp}	25 (stiffer) 12.5 (softer)	kNs/m
Slab bending stiffness	EI_{slab}	30	MN m^2
Slab mass per unit length	m_{slab}	580	kg/m
Slab width	b_{s}	1.2	m
Slab thickness	h_{s}	0.2	m
Foundation bed stiffness	k_{f}	200	MN/m^3
Foundation bed damping	c_{f}	164	kNs/m^3

where $\widetilde{\mathbf{K}}_r = \mathbf{K}_{rr} - \mathbf{K}_{rp}\mathbf{K}_{pp}^{-1}\mathbf{K}_{pr}$ is the stiffness matrix corresponding to the ROM of the layered subgrade. The size of $\widetilde{\mathbf{K}}_r$ is $r \times r$, where r corresponds to the total number of sleepers (i) multiplied by the number of retained DOFs per sleeper (here, $q = 6$).

The assembled track stiffness matrix for the ballasted side of the transition zone model, $\mathbf{K}^{\text{t,bal}}$, includes contributions from the rail, rail pads, sleepers, ballast, and subgrade. Schematically, $\mathbf{K}^{\text{t,bal}}$ can be expressed as:

$$\mathbf{K}^{\text{t,bal}} = \begin{bmatrix} \mathbf{K}_{\text{rail}} + \mathbf{K}_{\text{rail pad}} & -\mathbf{K}_{\text{rail pad}} & 0 \\ -\mathbf{K}_{\text{rail pad}} & \mathbf{K}_{\text{sleeper}} + \mathbf{K}_{\text{rail pad}} + \mathbf{K}_{\text{ballast}} & -\mathbf{K}_{\text{ballast}} \\ 0 & -\mathbf{K}_{\text{ballast}} & \mathbf{K}_{\text{ballast}} + \widetilde{\mathbf{K}}_{\text{r}} \end{bmatrix} \tag{4}$$

Here, $\mathbf{K}_{\text{rail}}$ represents the linear stiffness matrix for the rail elements, $\mathbf{K}_{\text{rail pad}}$ the linear stiffness matrix for the rail pads connecting the rail to the sleepers, $\mathbf{K}_{\text{sleeper}}$ the linear stiffness matrix for the sleeper elements, $\mathbf{K}_{\text{ballast}}$ the non-linear stiffness matrix for the ballast layer connecting the sleepers to the ballast masses, and $\widetilde{\mathbf{K}}_r$ the linear stiffness matrix for the layered subgrade (ROM).

The corresponding subgrade damping matrix is calculated using a Rayleigh damping approach. The reduced damping matrix $\widetilde{\mathbf{C}}_r$ is defined as a linear combination of the ballast mass matrix $\mathbf{M}_{\text{bal}}$ and the ROM stiffness matrix $\widetilde{\mathbf{K}}_r$:

$$\widetilde{\mathbf{C}}_r = \alpha\,\mathbf{M}_{\text{bal}} + \beta\,\widetilde{\mathbf{K}}_r \tag{5}$$

The Rayleigh coefficients, α and β, are determined by solving the system of equations in (6) to achieve 2% proportional damping at the boundaries of the primary frequency range of the model, here taken as 1 Hz and 25 Hz. This corresponds to $\xi_m = \xi_n = 0.02$, $\omega_m = 6.28$ rad/s, and $\omega_n = 157$ rad/s:

$$\begin{bmatrix} 1 & \omega_m^2 \\ 1 & \omega_n^2 \end{bmatrix} \begin{bmatrix} \alpha \\ \beta \end{bmatrix} = \begin{bmatrix} 2\xi_m\omega_m \\ 2\xi_n\omega_n \end{bmatrix} \tag{6}$$

The vehicle model employed in this study represents an iron ore wagon used for heavy haul traffic on the Iron Ore Line in the north of Sweden, cf. [9]. It comprises one car body and two three-piece bogies, each consisting of a bolster, two side frames, and two wheelsets. The vehicle model (see Fig. 2) has 14 DOFs: two for the vertical displacement and pitch rotation of the car body, four for the displacements and rotations of the side frames (two per bogie), four for the vertical displacements of the wheelsets, and four massless DOFs (one per wheelset) that interface with the rail, cf. [5]. The vehicle speed is 60 km/h, and the axle load is 30 tonnes. As vertical settlement is governed primarily by the vertical sleeper–ballast contact stresses generated under traffic loading, the adopted 2D vehicle model captures the most relevant dynamic effects, namely the vertical axle loads and the vertical displacements and pitching motions of the vehicle car body and bogies. Lateral displacements and yaw rotations of the vehicle are not considered in the present study.

Vertical dynamic vehicle–track interaction

Since the vehicle and track models are non-linear, the simulation of vertical dynamic vehicle–track interaction is conducted through direct integration in the time domain. A summary of the procedure is given here. For further details, see [5,6]. An extended state–space vector, $\mathbf{z}(t)$, is introduced as

$$\boldsymbol{z}(t) = \left\{ \mathbf{x}^{\text{t,T}},\ \dot{\mathbf{x}}^{\text{t,T}},\ \mathbf{x}_{\text{a}}^{\text{v,T}},\ \mathbf{x}_{\text{b}}^{\text{v,T}},\ \dot{\mathbf{x}}_{\text{a}}^{\text{v,T}},\ \dot{\mathbf{x}}_{\text{b}}^{\text{v,T}},\ \hat{\mathbf{F}}_{\text{a}}^{\text{T}}(t) \right\} \tag{7}$$

It includes the nodal displacements and rotations $\mathbf{x}^{\text{t}}$ and corresponding velocities $\dot{\mathbf{x}}^{\text{t}}$ of the assembled transition zone track model. The vertical displacements and velocities of the four massless DOFs of the vehicle model, cf. Fig. 2(a), interfacing the rail, are collected in the 4×1 vectors $\mathbf{x}_{\text{a}}^{\text{v,T}}$ and $\dot{\mathbf{x}}_{\text{a}}^{\text{v,T}}$, respectively, while $\mathbf{x}_{\text{b}}^{\text{v,T}}$ and $\dot{\mathbf{x}}_{\text{b}}^{\text{v,T}}$ are two 10×1 vectors containing the vertical displacements and velocities of the non-interfacial vehicle DOFs. Further, it contains the impulses of the wheel–rail contact forces, collected in the 4×1 vector as

$$\hat{\mathbf{F}}_{\text{a}}(t) = \int \mathbf{F}_{\text{w/r}}(t)\,\text{d}t \tag{8}$$

All the equations of motion for the vehicle and track, and the algebraic constraint equations coupling the vehicle and track, are assembled in one first-order matrix form as

$$\mathbf{A}(\boldsymbol{z},t)\,\dot{\boldsymbol{z}} + \mathbf{B}(\boldsymbol{z},t)\,\boldsymbol{z} = \mathbf{F}(\boldsymbol{z},t) \tag{9}$$

with

$$\mathbf{A}(\boldsymbol{z},t) = \begin{bmatrix} \mathbf{0} & \mathbf{M}^{\text{t}} & \mathbf{0} & \mathbf{0} & \mathbf{0} & \mathbf{0} & -\mathbf{N}^{\text{T}} \\ \mathbf{I} & \mathbf{0} & \mathbf{0} & \mathbf{0} & \mathbf{0} & \mathbf{0} & \mathbf{0} \\ \mathbf{0} & \mathbf{0} & \mathbf{0} & \mathbf{0} & \mathbf{0} & \mathbf{0} & \mathbf{I} \\ \mathbf{0} & \mathbf{0} & \mathbf{0} & \mathbf{0} & \mathbf{0} & \mathbf{M}_{\text{bb}}^{\text{v}} & \mathbf{0} \\ \mathbf{0} & \mathbf{0} & \mathbf{0} & \mathbf{I} & \mathbf{0} & \mathbf{0} & \mathbf{0} \\ \mathbf{T} & \mathbf{0} & \mathbf{0} & \mathbf{0} & -\mathbf{I} & \mathbf{0} & \mathbf{0} \\ \mathbf{R} & \mathbf{0} & -\mathbf{I} & \mathbf{0} & \mathbf{0} & \mathbf{0} & \mathbf{0} \end{bmatrix} \tag{10}$$

$$\mathbf{B}(\boldsymbol{z},t) = \begin{bmatrix} \mathbf{K}^{\text{t}} & \mathbf{C}^{\text{t}} & \mathbf{0} & \mathbf{0} & \mathbf{0} & \mathbf{0} & \mathbf{0} \\ \mathbf{0} & -\mathbf{I} & \mathbf{0} & \mathbf{0} & \mathbf{0} & \mathbf{0} & \mathbf{0} \\ \mathbf{0} & \mathbf{0} & \mathbf{K}_{\text{aa}}^{\text{v}} & \mathbf{K}_{\text{ab}}^{\text{v}} & \mathbf{0} & \mathbf{0} & \mathbf{0} \\ \mathbf{0} & \mathbf{0} & \mathbf{K}_{\text{ba}}^{\text{v}} & \mathbf{K}_{\text{bb}}^{\text{v}} & \mathbf{0} & \mathbf{C}_{\text{bb}}^{\text{v}} & \mathbf{0} \\ \mathbf{0} & \mathbf{0} & \mathbf{0} & \mathbf{0} & \mathbf{0} & -\mathbf{I} & \mathbf{0} \\ \mathbf{U} & \mathbf{0} & \mathbf{0} & \mathbf{0} & \mathbf{0} & \mathbf{0} & \mathbf{0} \\ \mathbf{S} & \mathbf{0} & \mathbf{0} & \mathbf{0} & \mathbf{0} & \mathbf{0} & \mathbf{0} \end{bmatrix} \tag{11}$$

Here, $\mathbf{M}^{\text{t}}$, $\mathbf{K}^{\text{t}}$, and $\mathbf{C}^{\text{t}}$ are the mass matrix, stiffness matrix, and viscous damping matrix of the complete track model, respectively, while $\mathbf{M}^{\text{v}}$, $\mathbf{K}^{\text{v}}$, and $\mathbf{C}^{\text{v}}$ are the corresponding matrices for the vehicle model. At each time step, each wheel–rail contact force is distributed as consistent forces and moments on the adjacent rail nodes using Hermitian interpolation polynomials contained in the block-diagonal matrix $\mathbf{N}$, cf. [5].

By assuming a prescribed vehicle speed $v(t)$ and considering the Coriolis and centripetal accelerations that occur because the vehicle model is moving along the track model, the constraints on the interfacial velocities and accelerations for the massless DOFs of the vehicle model are expressed in $\mathbf{R}$, $\mathbf{S}$, $\mathbf{T}$, and $\mathbf{U}$, cf. [5]. The mixed force vector $\mathbf{F}$ is written as

$$\mathbf{F}(\boldsymbol{z},t) = \left\{ \begin{bmatrix} \mathbf{F}_{\text{s/b}}^{\text{t,T}}(t) + \mathbf{F}_{\text{g}}^{\text{t,T}} & \mathbf{0} \end{bmatrix}^{\text{T}} \quad \mathbf{0}^{\text{T}} \quad \mathbf{F}_{\text{b}}^{\text{v,T}}(t) \quad \mathbf{0}^{\text{T}} \quad \dot{\mathbf{x}}^{\text{irr}} \quad \ddot{\mathbf{x}}^{\text{irr}} \right\}^{\text{T}} \tag{12}$$

where the vector $\mathbf{F}_{\text{s/b}}^{\text{t}}$ contains the state-dependent contribution to the sleeper–ballast contact forces acting at each sleeper node and (with opposite direction) on each ballast mass within the ballasted track section. The constant vector $\mathbf{F}_{\text{g}}^{\text{t}}$ represents the gravity load on the track superstructure. Prescribed external loads, such as vehicle weight, are assembled in $\mathbf{F}_{\text{b}}^{\text{v}}$, while $\mathbf{x}^{\text{irr}}$ denotes a prescribed relative wheel–rail surface displacement that may be used to simulate, for example, a wheel flat or a rail joint. Such surface irregularities are not considered in the present study. However, the model does incorporate evolving irregularities in the vertical track geometry (longitudinal level), arising from differential sleeper settlement under cumulative load passages, as well as the influence of voids that may develop beneath individual sleepers.

Track settlement

Track settlement depends on local site conditions and may originate either in the ballast or in the subgrade. Where a deep, soft subgrade is present, settlement is dominated by subgrade creep and consolidation, whereas in cases where a stiff, competent foundation exists beneath the ballast, a substantial proportion of the settlement occurs within the ballast layer and exhibits non-linear behaviour. Therefore, the iterative procedure, illustrated in Fig. 1, aims to calculate the degradation of track geometry due to long-term accumulated differential settlement of ballast and subgrade for a given traffic load (i.e., a specified number of wheel passages). The settlement (permanent displacement) in the ballast and subgrade layers is predicted using two empirical models, as described below.

Settlement in ballast layer — visco-plastic threshold model

In each iteration step j ($j = 1, 2, \ldots, n_{\text{s}}$), after solving the vertical dynamic vehicle–track interaction in the time domain, the time history of each sleeper–ballast contact force at each sleeper node is post-processed using the FE model. The incremental settlement $\delta_{i,q,j}$ [m] at

each sleeper i, with $i = 1, 2, \ldots, (N_{\text{bays}} - 1)$, and for each sleeper node $q = 1, 2, \ldots, 6$ (six nodes per half-sleeper), is expressed as a function of the corresponding maximum contact pressure $p_{\text{s/b},i,q}$ (considering the bottom surface area of the sleeper):

$$\delta^{\text{bal}}_{i,q,j} = \sum_{n=1}^{N_{\text{w}}} \left\{ \sum_{k=1}^{N_{\text{k}}} \alpha_k \left[\frac{\langle \max(p_{\text{s/b},i,q})_n - p_{\text{th},i,q} \rangle}{p_0} \right]^{\beta_k} \right\} \tag{13}$$

where N_{w} is the number of wheels in the vehicle model (here, $N_{\text{w}} = 4$), N_{k} is the order of the applied polynomial formulation for the ballast settlement model, α_{k} and β_{k} are empirical parameters, and $p_0 = 1$ kPa is a reference contact pressure [5,6]. In this settlement model, there is no accumulation of permanent ballast deformation if the maximum sleeper–ballast contact pressure generated by a passing wheel is below a certain threshold value $p_{\text{th},i,q}$, as reflected in Eq. (13) by the Macaulay brackets. The unit of α_{k} is here taken as mm/10^5 load cycles, see the discussion below. Consequently, for simulation purposes, it is sufficient to relate the number of load cycles to the number of train axles [23,39].

The accumulated settlement of the ballast layer for each sleeper number i and sleeper node q after n_{s} iterations (corresponding to N_{s} wheel passages) is then

$$\Delta^{\text{bal}}_{i,q}(n_{\text{s}}) = \sum_{j=1}^{n_{\text{s}}} \delta^{\text{bal}}_{i,q,j}. \tag{14}$$

In subsequent iterations, these accumulated settlements are applied in the updated track model by revising the breakpoint of each bi-linear sleeper–ballast contact stiffness, see Fig. 2(c). For each sleeper number i and sleeper node q, it is assumed that the current threshold $p_{\text{th},i,q}$ depends on $\Delta^{\text{bal}}_{i,q}$ according to

$$p_{\text{th},i,q}(\Delta^{\text{bal}}_{i,q}) = p_{\text{th},\infty} - \left(p_{\text{th},\infty} - p_{\text{th},0}\right) e^{-\gamma \Delta^{\text{bal}}_{i,q}}. \tag{15}$$

where $p_{\text{th},0}$ is the initial (virgin) threshold value before any traffic loading has been applied, $p_{\text{th},\infty}$ is the long-term threshold for a stabilised ballast layer, and γ determines the hardening rate. The hardening law for the threshold p_{th} has been presented in detail in our previous work, cf. [5]. As the settlement parameters are both site- and track-specific, the model parameters were calibrated against field measurements carried out on the Iron Ore Line in northern Sweden, cf. [6] and Section "Verification and assessment of settlement models".

Settlement in subgrade layers

For each sleeper number i and sleeper node q, the formula proposed by Li and Selig [29], and later modified by Charoenwong et al. [40], is used to predict the increment in permanent deformation of each subgrade layer

$$\Delta\varepsilon^{p}_{i,q,j}(y) = \frac{a}{100} \left(\frac{\sigma_{\text{d}}(y)}{\sigma_s(y)} \right)^{m} \left(N_j^b - N_{j-1}^b \right) \tag{16}$$

where $\Delta\varepsilon^{p}_{i,q,j}(y)$ is the plastic strain increment in the subgrade at depth y, $\sigma_{\text{d}}(y)$ denotes the corresponding deviatoric stress due to traffic load (N/m^2), see Equation (17), while N_j is the total number of wheel passages including iteration j, and N_{j-1} is the total number of wheel passages including iteration $j-1$. $\sigma_s(y)$ represents the shear strength of the soil layer at depth y (N/m^2), while a, b and m are parameters that depend on the subgrade soil type. Table 2 presents the values of these parameters for four different soil types.

The deviatoric stress at depth y is determined using the extended form of the Flamant solution [31], which provides analytical expressions for stresses induced by a surface unit load on a layered soil subgrade provided that the difference between soil layers are not substantial. The applied surface load corresponds to the maximum sleeper–ballast contact force, generated by each of the four wheels in the vehicle model, at each sleeper i and sleeper node q. For each sleeper node, it is assumed that the resulting distribution of deviatoric stress is dominated by the contribution from the load acting on that node, while the contribution from loads acting on adjacent nodes can

Table 2
Parameters a, b, and m for different subgrade soils.
Source: Adapted from [29].

Subgrade soil type	a	b	m
Silt	0.64	0.06–0.17	1.4–2.0
Silt of high plasticity	0.84	0.08–0.19	1.3–4.2
Clay of low plasticity	0.30–3.5	0.08–0.34	1.0–2.6
Clay of high plasticity	0.82–1.5	0.12–0.27	1.3–3.9

be neglected. This assumption is in line with previous work [27]. The present approach also neglects the influence of principal stress rotation on the track response [23]. It has been shown, through comparisons between solutions for layered soils and those for homogeneous soil, that the distribution of vertical stress is not highly sensitive to material properties, provided that the differences in the soil properties between layers are not substantial [31]. Moreover, by subdividing the subgrade into smaller depth intervals and accounting for the induced vertical stresses from the external loading and the weight of the overlying layers, a reliable approximation of the deviatoric stress at different depths can be achieved [31]. It should be noted that the deviatoric stress is treated as a scalar. Consequently, both the deviatoric stress and the generation of plastic strains in the soil are considered solely in the loading direction. The deviatoric stress is calculated as

$$\sigma_{\text{d}}(y) = \frac{\sqrt{(\sigma_{xx} - \sigma_{yy})^2 + (\sigma_{xx} - \sigma_{zz})^2 + (\sigma_{yy} - \sigma_{zz})^2 + 6\left(\tau_{xy}^2 + \tau_{yz}^2 + \tau_{xz}^2\right)}}{\sqrt{2}} \tag{17}$$

The depth-dependent shear strength of the soil is calculated using the classical Mohr–Coulomb failure criterion. Here, the vertical effective geostatic stress at depth y within layer l is expressed as

$$\sigma_{\text{w}}(y) = \gamma_{\text{ball}}\, h_{\text{ball}} + \sum_{i=1}^{l-1} \gamma_i\, h_i + \gamma_l \left(y - \sum_{i=1}^{l-1} h_i \right), \tag{18}$$

where γ_{ball} and h_{ball} are the unit weight and thickness of the ballast layer, γ_i and h_i denote the unit weight and thickness of the overlying soil layers, and γ_y and h_y represent the corresponding properties of the current soil layer. In this formulation, the stress at depth y is obtained as the sum of three contributions: the surcharge from the ballast, the cumulative weight of all overlying layers, and half of the weight of the current layer, ensuring that the stress is taken at its mid-depth. The resulting maximum shear strength of the soil at depth y is given by the Coulomb failure criterion:

$$\sigma_s(y) = \sigma_{\text{w}}(y) \tan\varphi_y + c_y, \tag{19}$$

where y denotes the vertical depth coordinate. The parameters φ_y and c_y represent the internal friction angle and effective cohesion, respectively, of the soil layer in which the depth y is located. These parameters are assumed to be constant within each soil layer. In all these considerations the soil has been simplified as a single-phase medium. Under drained conditions in coarse-grained materials, the calculated total stress becomes equal to the effective stress, and the shear strength becomes a function of depth. In contrast, in fine-grained materials such as clay, the shear strength becomes independent of the vertical stress, and the cohesion should be taken as equal to the undrained shear strength.

As described in [41], plastic strain in railway subgrade soils is predominantly induced by low-frequency vibrations. Under such loading, the number of loading cycles corresponds directly to the number of axle passages. Consequently, the settlement of railway tracks or subgrade layers can be determined using the layer-wise summation method, as expressed in Eq. (20). In the present study, the subgrade is discretised into H_k elements along the depth direction, each with a corresponding height h_k. The plastic strain increment in each element is evaluated

using Eq. (16). In iteration step j, the increment of the total permanent deformation of the layered subgrade, $\delta^{\text{sub}}_{i,q,j}$, is computed as in Eq. (20):

$$\delta^{\text{sub}}_{i,q,j} = \sum_{k=1}^{H_k} \left(\Delta\varepsilon^{p}_{i,q,j}(k) \right) h_k \tag{20}$$

The accumulated settlement of the layered subgrade for each sleeper number i and sleeper node q after n_s iterations (corresponding to N_s wheel passages) is

$$\Delta^{\text{sub}}_{i,q,j}(n_s) = \sum_{j=1}^{n_s} \delta^{\text{sub}}_{i,q,j} \tag{21}$$

The total settlement (per iteration step and accumulated, respectively) at each sleeper node is determined by summing the settlements in the ballast layer and the subgrade

$$\delta^{\text{total}}_{i,q,j}(n_s) = \delta^{\text{sub}}_{i,q,j} + \delta^{\text{bal}}_{i,q,j}(n_s) \tag{22}$$

$$\Delta^{\text{total}}_{i,q,j}(n_s) = \Delta^{\text{sub}}_{i,q,j} + \Delta^{\text{bal}}_{i,q,j}(n_s) \tag{23}$$

In each iteration step, up to 10^5 load cycles (corresponding to 3 MGT of traffic with the loaded iron ore trains) are considered. However, an adaptive step length is applied such that the maximum allowed settlement increment per iteration, $\delta^{\max}$, is not exceeded. If $\max(\delta^{\text{total}}_{i,q,j}) > \delta^{max}$, all $\delta_{i,q,j}$ are scaled linearly:

$$\delta^{\text{total}}_{i,q,j} = \frac{\delta^{max}}{\max(\delta^{\text{total}}_{i,q,j})}\, \delta^{\text{total}}_{i,q,j}, \tag{24}$$

and the number of load cycles in iteration step j is given by

$$N_{s,j} = \frac{\delta^{max}}{\max(\delta^{\text{total}}_{i,q,j})} \cdot 10^5. \tag{25}$$

If $\max(\delta^{\text{total}}_{i,q,j}) \le \delta^{max}$, then $N_{s,j} = 10^5$. This procedure limits abrupt changes in the resulting distribution of differential settlement between iterations. In this study, $\delta^{\max}$ is taken as 0.2 mm; see Nielsen and Li [42].

Results and discussion — short-term dynamic response

In this section, the methodology used to predict the dynamic vehicle–track interaction in a railway transition zone is presented. In this application, the track model represents the transition between a ballasted track on an embankment (with lower track stiffness at rail level) and a slab track on a bridge or in a tunnel (with higher track stiffness at rail level). Both directions of vehicle travel are considered. The simulations include three different scenarios corresponding to different transition zone designs, as shown in Fig. 4.

As shown in Fig. 4(a), Scenario 1 is the reference case without any measure to mitigate the stiffness gradient at the transition. In Scenario 2, shown in Fig. 4(b), the stiffness gradient is mitigated by introducing a transition wedge (with a layer of higher stiffness in the subgrade) on the ballasted side between sleepers 1 and 32. This measure also introduces another, smaller stiffness gradient at the transition between the conventional ballasted track on the embankment and the ballasted track on the transition wedge. Scenario 3 is identical to Scenario 1 except that the rail pad stiffness on the slab side is reduced by half. This reduces the track stiffness at rail level on the slab track side, resulting in a smaller stiffness gradient at the transition between the two track forms.

The differences between vehicle travel directions, (i) from the softer to the stiffer track form, and (ii) from the stiffer to the softer track form, are also investigated. As illustrated in Fig. 2, the components of the ballasted track comprise rail, sleepers, ballast, and subgrade. The slab track consists of a concrete slab beam supported by a Winkler foundation on a rigid bridge. The **Substructure* generate command in ABAQUS is used to obtain the static stiffness matrix of the substructure on the ballasted track side, thereby representing the layered subgrade, including any mitigation measures designed to achieve a prescribed stiffness gradient, by means of a ROM. Note that the so-called internal modes of the linear 3D FEM model, as also provided by ABAQUS, are neglected here because the maximum frequency of interest is limited to approximately 25 Hz. The selected parameters for the layered subgrade model are shown in Table 3. It should be noted that subgrade layer 3 consists of a softer material than the overlying layers.

Table 3
Soil properties with representative small-strain stiffness values for the layered substructure, selected for the simulations in Sections Results and discussion – Short-term dynamic response and Results and discussion – Long-term differential settlement. Note that the ballast is not included in the ROM representation of the 3D FE subgrade model.

Layer	H (m)	ρ (kg/m^3)	ν	E (MPa)	φ' (°)	c' (kPa)
Ballast	0.5	1800	0.25	150	55	0
Sub-ballast	0.4	2000	0.25	120	45	0
Subgrade layer 1	0.6	2000	0.25	150	32	5
Subgrade layer 2	3.0	2000	0.25	100	31	5
Subgrade layer 3	2.0	2000	0.25	60	30	10
Subgrade layer 4	4.0	2000	0.25	300	35	10

Track receptance

The point receptance of the rail was calculated for the ballasted track in the absence of sleeper voids (linear track model). The rail was excited vertically at mid-span between two sleepers, and the rail receptance was evaluated in sleeper bay 10, both with and without a transition wedge (see Fig. 5). Within the frequency range up to 500 Hz, two dominant resonances and one anti-resonance are observed. At the first resonance frequency (30 Hz), the rail and sleepers oscillate in phase, whereas at the second resonance (320 Hz) they vibrate out of phase. As expected, the transition wedge reduces the static receptance (i.e., it increases the track stiffness at rail level), and the first resonance (around 30 Hz in Scenario 1) shifts to a higher frequency (around 70 Hz in Scenario 2).

Static track stiffness at rail level

Vertical static track stiffnesses at rail level along the transition zone for Scenarios 1 to 3 are compared in Fig. 6. The track stiffness displays a distinct periodic pattern, indicative of the discrete spacing of the rail supports.

The analysis demonstrates that Scenario 2 provides a gradual, stepwise variation in stiffness along the track. In this scenario, the maximum stiffness gradient is reduced by approximately 40% relative to Scenario 1, thereby alleviating the abrupt stiffness change observed in Scenario 1. This improvement is expected to influence dynamic vehicle loading, differential settlement, and the overall long-term performance of the transition. Likewise, the use of softer rail pads on the stiffer track form helps to reduce the stiffness gradient.

Interaction between retained DOFs

The influence of the dynamic interaction between adjacent sleepers, via the substructure, has been investigated using various track models in previous studies. For example, in simplified 2D models, a layer of ballast masses combined with shear springs and dampers between the ballast masses has been considered, see, e.g., Oscarsson et al. [43]; Zhai et al. [44]). Ballast acceleration levels in 2D track models have been reported to be overestimated if a shear coupling between the ballast masses is neglected. Subsequently, Nasrollahi et al. [6] demonstrated that incorporating the interaction between sleepers via the ballast and subgrade improves the agreement between measured and simulated dynamic responses in a transition zone model.

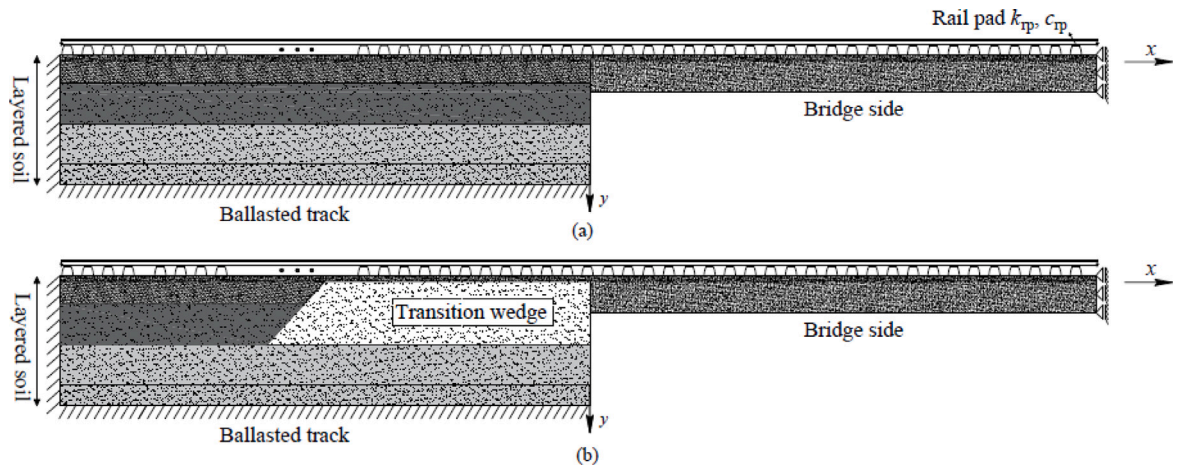

Fig. 4. Schematic illustration of the simulated scenarios: (a) Scenario 1, the reference case without any mitigation measure; (b) Scenario 2, in which the stiffness gradient is mitigated by introducing a transition wedge in the subgrade on the ballasted side between sleepers 1 and 32; and (c) Scenario 3, which is identical to Scenario 1 except that the rail pad stiffness on the slab track side is reduced by half.

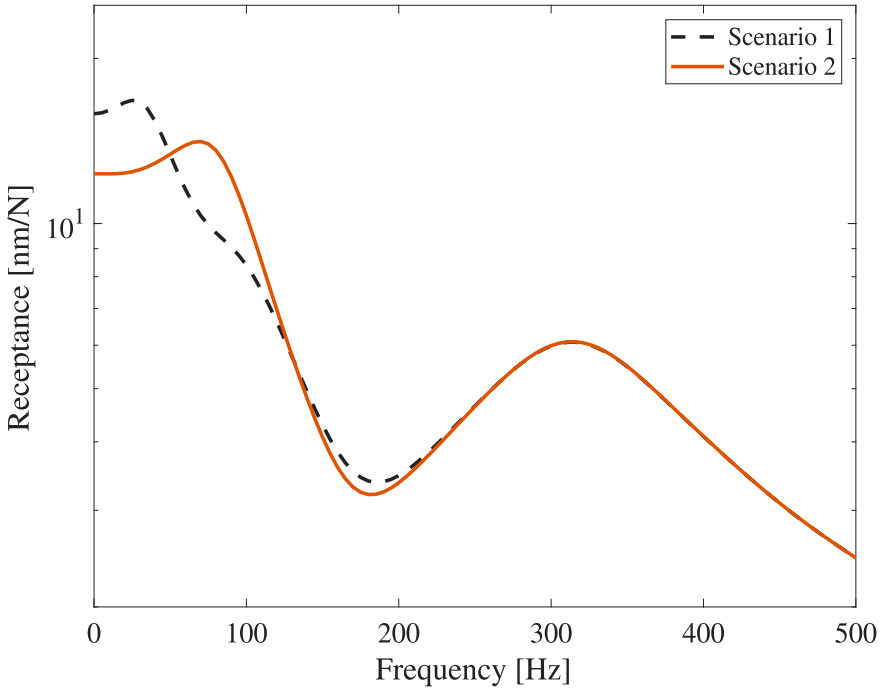

Fig. 5. Point receptance of the rail at sleeper mid-span: comparison between receptances in sleeper bay 10 for Scenarios 1 and 2.

In the present study, the influence of the interaction between adjacent sleepers, transmitted through the subgrade, on the predicted rail receptance has been evaluated. This was investigated by considering different numbers of off-diagonals in the ROM stiffness matrix. For example, if only the interactions between sleepers i-1, i, and i+1 (i=1, 2, …, N_{bays}-1) via the layered subgrade are considered, then all off-diagonal terms coupling the retained DOFs associated with sleeper i to the retained DOFs associated with sleepers ..., i-3, i-2, and i+2, i+3, …, are neglected. In Fig. 7, the calculated receptance is presented for different scenarios of sleeper interaction, considering 1, 2, 3, or 5 sleepers on either side of any given sleeper. The example described above corresponds to the case labelled as '1 sleeper' in the legend. The receptance is found to converge as more sleeper interactions are included, indicating that interactions beyond five sleepers on either side are negligible. Consequently, in the subsequent analyses in this paper, the configuration including five sleepers on either side of any given sleeper is applied in order to reduce computational time.

Wheel–rail contact force

The influence of the stiffness gradients in transition zone design scenarios 1 to 3 on the wheel–rail contact force for the leading wheel is illustrated in Fig. 8. Both vehicle travel directions are considered. Scenario 1 without mitigation measure leads to the highest contact force maxima. For the travel direction from the softer track form to the stiffer track form, the maximum contact force is generated at the transition, see Fig. 8(a), while for the opposite travel direction, the maximum force is generated around sleepers 6 to 8 on the ballasted side, cf. Fig. 8(b). Nevertheless, the magnitude of the maximum contact force is similar for both travel directions.

With a transition wedge installed on the ballasted side (Scenario 2), the maximum wheel–rail contact force at the transition (vertical dashed line) between the two track forms is reduced by approximately 0.5 kN. A second local maximum in the contact force is generated at the far end of the wedge. It should be emphasised that these results

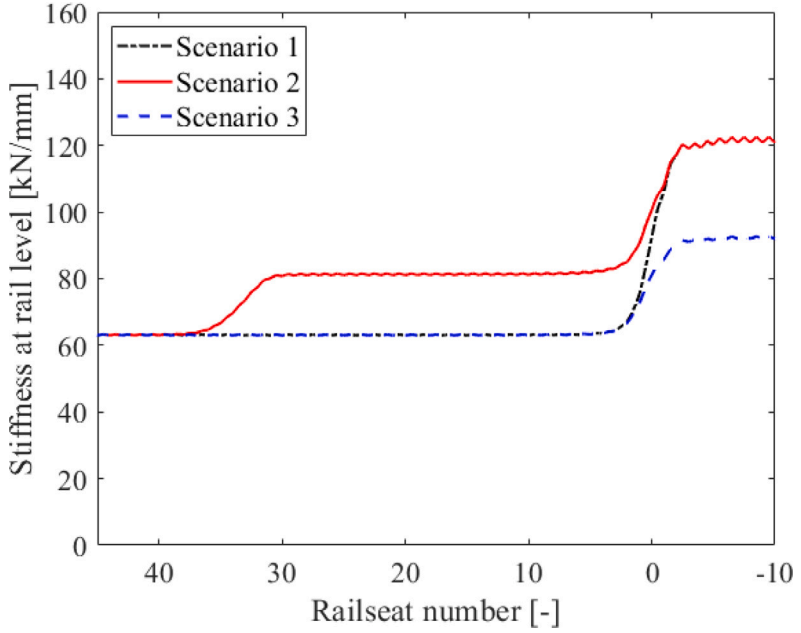

Fig. 6. Static track stiffness at rail level along the transition with and without a transition zone design: Scenario 1, without any mitigation; Scenario 2, with a transition wedge; and Scenario 3, with softer rail pads on the slab track side.

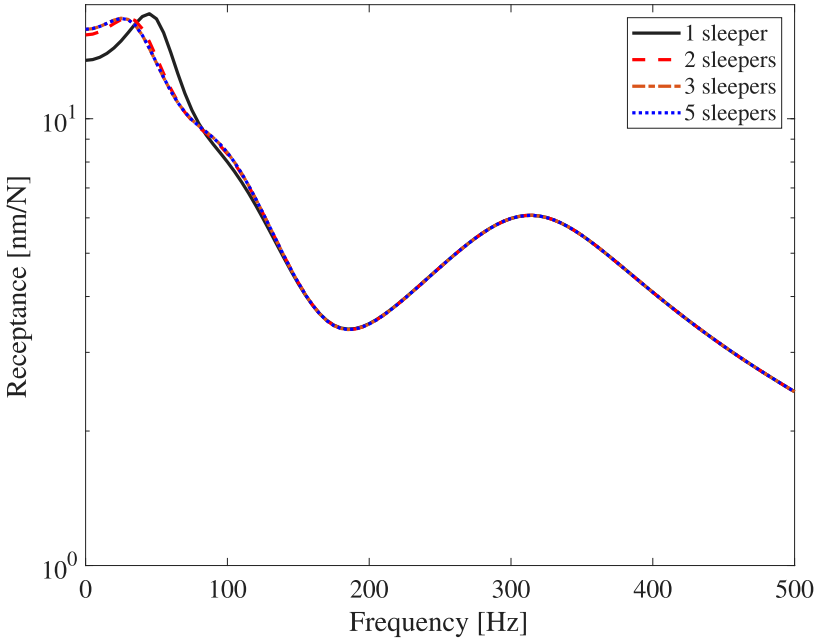

Fig. 7. Influence of number of sleepers interacting via the subgrade on the point rail receptance above sleeper 25 on the ballasted side.

correspond to the first vehicle passage in the first iteration step. After subsequent vehicle passages, as the differential settlement between the two track forms becomes more pronounced, the difference in contact force between scenarios will progressively increase. Similarly, in the case where softer rail pads are installed on the stiffer track form (Scenario 3), the maximum contact force is reduced relative to Scenario 1.

Rail seat load along the transition zone

Based on calculated time histories, the maximum rail seat loads, evaluated across all sleepers along the transition zone for the three different scenarios, are shown in Fig. 9. For Scenario 1, without a mitigation measure, a substantial variation in the simulated maximum rail seat load is observed between sleepers 1 to 5 near the transition, compared to the more uniform distribution of load between the sleepers farther away from the transition. The scenarios featuring softer rail pads or a transition wedge demonstrate a better distribution of load between sleepers, especially for sleepers 1 to 5. However, in the case of the transition wedge, the additional stiffness gradient at sleeper 33, cf. Fig. 6, leads to another local maximum in rail seat load.

The lower rail seat loads immediately before the transition, followed by an abrupt increase just after the transition (on the stiffer track form, which is not shown here), indicate that sleepers 1 and 2 are being suspended by the section of rail located on the stiffer track form, thereby preventing significant displacement. As a result, the load is

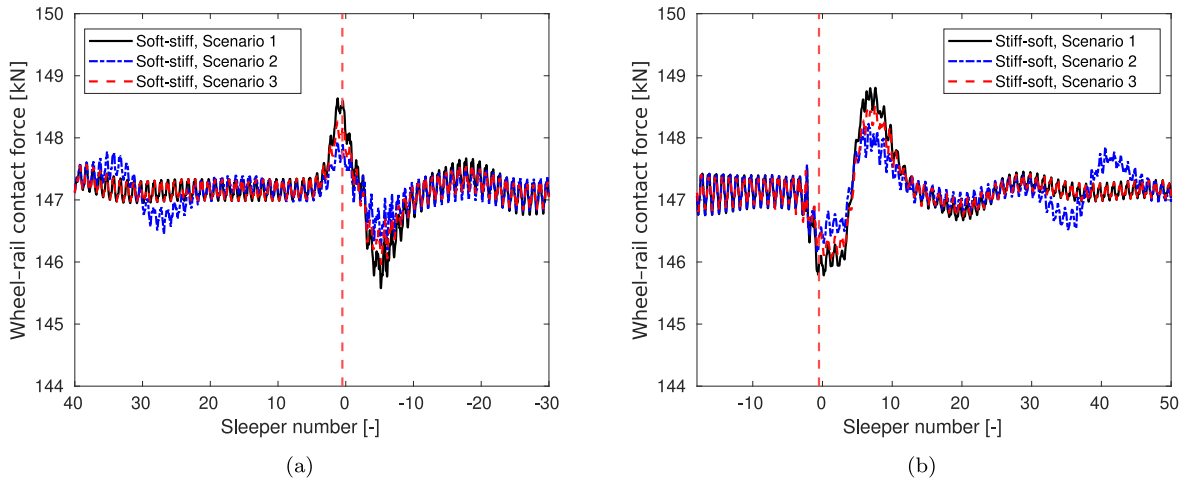

Fig. 8. Influence of different transition zone designs on the time history of wheel–rail contact force along the transition. The vertical line indicates the position of the transition. Vehicle travel direction (a) from the softer track form to the stiffer track form, (b) from the stiffer track form to the softer track form.

redistributed among the adjacent sleepers. This phenomenon occurs in conjunction with higher dynamic vehicle loading, induced by the low-frequency pitching motion of the vehicle as it traverses the stiffness gradient and the evolving misalignment in rail level at the transition.

Sleeper–ballast contact stress and sleeper displacement

Based on calculated time histories, Fig. 10(a) compares the maximum sleeper–ballast contact pressure along sleeper 10 for the two scenarios of transition zone design during the passage of an iron ore vehicle. Generally, it is observed that the maximum stress is generated adjacent to the rail seat of the sleeper, which is at longitudinal position 0.75 from the sleeper centre. The pressures at the sleeper end (1.25 m) and at sleeper centre (0 m) are lower. For sleeper 10, the maximum contact pressure in Scenario 2 is greater than that in Scenario 1, resulting in higher sleeper–ballast contact stresses when the transition wedge design is applied. This is because Scenario 2 involves a higher support stiffness, leading to a more narrow distribution of load along the track. This can be anticipated to increase the contribution of ballast settlement. On the other hand, because the subgrade is stiffer in Scenario 2, a lower contribution from the subgrade settlement is expected. This will be further examined in Section "Results and discussion — Long-term differential settlement".

Similarly, the maximum sleeper node displacements caused by the passage of a vehicle are presented in Fig. 10(b). The bending of the sleeper is observed with a maximum displacement at the railseat. As expected, the transition wedge in Scenario 2 results in a lower displacement of sleeper 10.

Results and discussion — long-term differential settlement

Long-term accumulated differential settlements in a transition zone, with or without measures to mitigate the stiffness gradient, have been simulated up to a traffic load of 15 MGT (approximately one year of operation with the loaded iron ore trains, corresponding to 500 000 wheel passages). The settlement at each sleeper node across the transition zone, with each sleeper being discretised into five beam elements, has been determined using the two settlement models presented in Section "Track settlement".

Verification and assessment of settlement models

The viscoplastic threshold model used to predict settlement in the ballast layer was calibrated and validated against measured data from a transition zone on the Iron Ore Line, as reported in Nasrollahi et al. [5,6]. The predicted long-term settlement, obtained using the calibrated set of input parameters, showed good agreement with the field measurements, with deviations of approximately 10% (or less). The Li and Selig formula [29] for predicting long-term settlement in subgrade layers has been widely adopted in the literature, see for example [27,40,45].

As described in Section "Settlement in subgrade layers", the deviatoric stress for each element is calculated using Flamant's equations. These results are verified here against those obtained from the 3D FE model simulated in the commercial finite element software Abaqus. Fig. 11 shows the calculated deviatoric stress as a function of depth for a load case in which the maximum simulated contact force between sleeper 35 and the ballast layer is applied as a single concentrated (static) load at the interface between the ballast layer and the layered subgrade. This load is applied on the subgrade surface directly beneath sleeper 35, see Fig. 2. No transition zone design intended to mitigate the stiffness gradient was considered in this simulation. The good agreement shown in Fig. 11 demonstrates that the Flamant's equations can be adopted to substantially reduce the simulation time required for post-processing the deviatoric stresses, instead of relying on the full FE model of the subgrade.

For the transition wedge design illustrated in Fig. 3, the resulting distribution of shear strength within the soil layers as a function of depth for sleepers 10, 32, 36, and 46, selected here as representative sleepers along the transition zone and calculated using Eq. (19), is shown in Fig. 12. Sleeper 10 is located above the centre of the cubic section of the transition wedge, while sleepers 32 and 36 are positioned above its inclined section. Sleeper 46 serves as a reference point situated well beyond the wedge. At the interface between the ballast and sub-ballast layers ($y = 0$), the shear strength σ_s is due to the applied ballast surcharge weight. With increasing depth, the shear strength progressively increases due to increase in vertical overburden and the stress-dependent shear strength. The results indicate that sleepers located on the transition wedge (Sleepers 10, 32, and 36) exhibit slightly higher strength values at shallower depths compared to the reference sleeper (Sleeper 46). This demonstrates that the weight of the wedge increases the strength of the layered soil beneath it, thereby strengthening the underlying strata and consequently reducing settlement in these layers. A higher ratio between the current deviatoric stress and the reference shear strength, which itself depends on the vertical stress at that depth, results in lower plastic strain. The rate of this increase depends on the soil properties (γ, φ, c) of each successive layer. This formulation provides a physically consistent representation of strength variation in stratified soil deposits, and serves as the foundation for the subsequent analysis of the settlement in the subgrade.

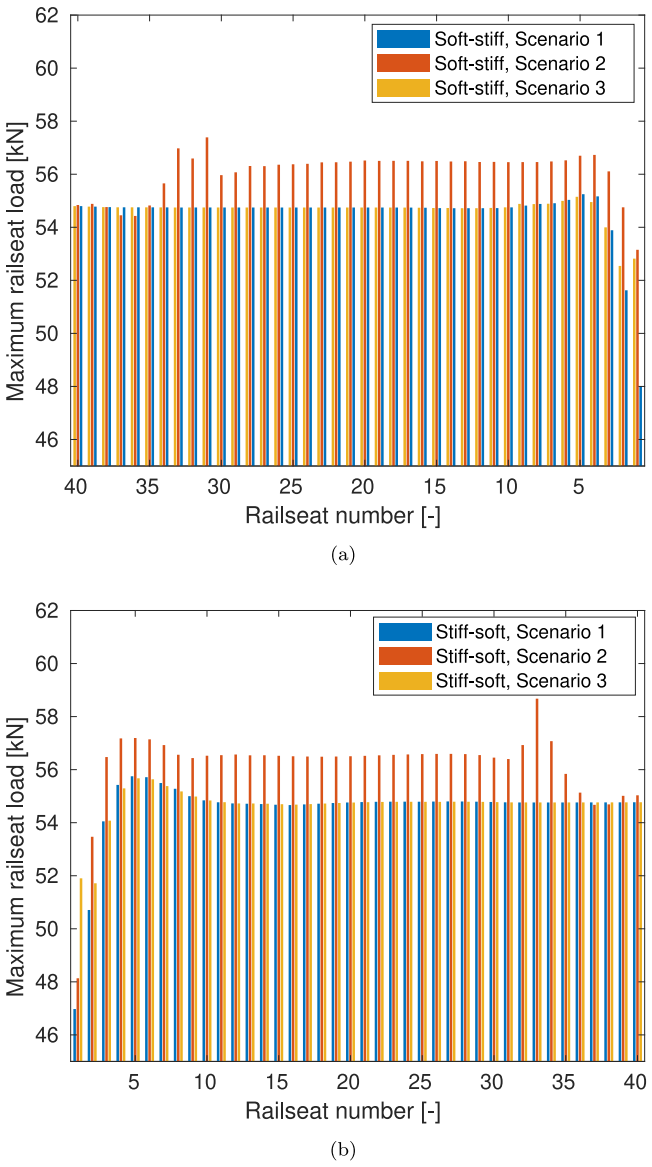

Fig. 9. Maximum rail seat loads along the track model during a vehicle passage. Vehicle travel direction (a) from the softer track form to the stiffer track form, (b) from the stiffer track form to the softer track form. Transition is located at 0.

Using the empirical settlement models described in Section "Track settlement", a parametric study was conducted to illustrate the respective contributions of the ballast layer and the layered subgrade to the overall accumulated settlement at selected sleepers along the transition zone. The input parameters applied in the visco-plastic threshold settlement model were taken from [6] and set to: $\alpha_k = 0.02\,[\mathrm{mm}/10^5$ load cycles], $\beta_k = 2.8$, $p_{\mathrm{th},0} = 90\,\mathrm{kPa}$, $p_{\mathrm{th},\infty} = 240\,\mathrm{kPa}$, and $\gamma = 0.15\,[1/\mathrm{mm}]$. For the subgrade settlement prediction model, the parameters a, b, and m used in Eq. (16) are listed in Table 4. These values were obtained by averaging the ranges specified in Table 2. In this study, the settlements in the bottom layer (Layer 4) of the subgrade and in the transition wedge are neglected, due to the higher stiffness of these layers.

For scenario 2, time histories of sleeper–ballast contact pressure beneath the representative sleepers 10, 32, 36, and 46 were computed using the results from the first iteration with the short-term model of dynamic vehicle–track interaction. Long-term differential settlement in the transition zone was then predicted for one year of traffic, assuming

Table 4
Parameter values of the subgrade settlement prediction model.

Layer	a	b	m
Sub-ballast	0.84	0.17	1.5
Subgrade layer 1	0.64	0.17	1.5
Subgrade layer 2	0.54	0.11	1.3
Subgrade layer 3	1.00	0.25	1.8
Subgrade layer 4	0.00	0.00	0.0
Transition wedge	0.00	0.00	0.0

that the respective maximum sleeper–ballast contact pressure below each sleeper remained constant. Based on these simplified load assumptions and using the two empirical settlement models in Section "Track settlement", Fig. 13 illustrates the load cycle histories of settlement contributions in the ballast and subgrade, respectively. As expected, settlement rates in both layers decrease with increasing numbers of wheel passages. For sleeper 10 that is centred on the transition wedge (Fig. 13(a)), the settlement of the ballast layer is higher than elsewhere owing to the higher track stiffness leading to higher vehicle dynamic loading and increased sleeper–ballast contact pressure (see Fig. 9(a)). In contrast, in the subgrade the settlement is significantly lower because of the presence of stiffer material within the transition wedge that reduces the dynamic deviatoric stress. At the inclined edge of the transition wedge, the contribution from settlement in the subgrade increases. Beyond the transition wedge at sleeper 46, the settlement of the ballast layer is smaller, owing to greater track flexibility and lower sleeper–ballast contact pressures, whereas the subgrade settlement is larger because of the softer underlying layers.

Influence of transition zone design on long-term settlement

For the considered vehicle loading (axle loads 30 tonnes and speed 60 km/h), and the adopted parameter sets in the settlement models for the ballast and subgrade, the analysis predicts a monotonic accumulation of settlement beneath all sleeper nodes in the ballasted track section. However, the stiffness gradient at the transition, along with any misalignment in longitudinal rail level between the two track forms (for example, due to early compaction of the ballast layer) induces a dynamic excitation of the vehicle–track system. This excitation results in a pitching motion of the vehicle and consequently higher sleeper–ballast contact pressures at some sleepers a few metres from the transition. A feedback loop is established, where the increased dynamic excitation leads to elevated sleeper–ballast contact pressures and further settlement, thereby exacerbating differential degradation within the transition zone.

Two traffic-direction scenarios are analysed: (i) loaded iron ore trains travelling from the softer track section to the stiffer section, and (ii) traffic in the opposite direction. The effectiveness of the two studied transition zone design interventions, i.e., the transition wedge on the ballasted side and the use of lower-stiffness rail pads on the stiffer track form, is evaluated based on their ability to mitigate long-term differential settlements.

Fig. 14 presents the predicted rail displacement due to gravity load (but excluding vehicle load), resulting from the accumulated differential sleeper settlement after 15 MGT of traffic. The results indicate a misalignment in rail level between the two track forms, primarily because settlement on the stiffer track form has been neglected compared to the settlement of the ballast and subgrade on the ballasted side. The maximum settlement observed near sleeper 8 or sleeper 5, depending on travel direction, is associated with the generated pitching motion of the vehicle as it passes over the transition. This mechanism has been reported in previous studies; cf. [5]. Specifically, the stiffness gradient induces a pitching motion of the two bogies and the car body, which generates a transient dynamic loading along the track and a local increase of the sleeper–ballast contact forces adjacent to the transition.

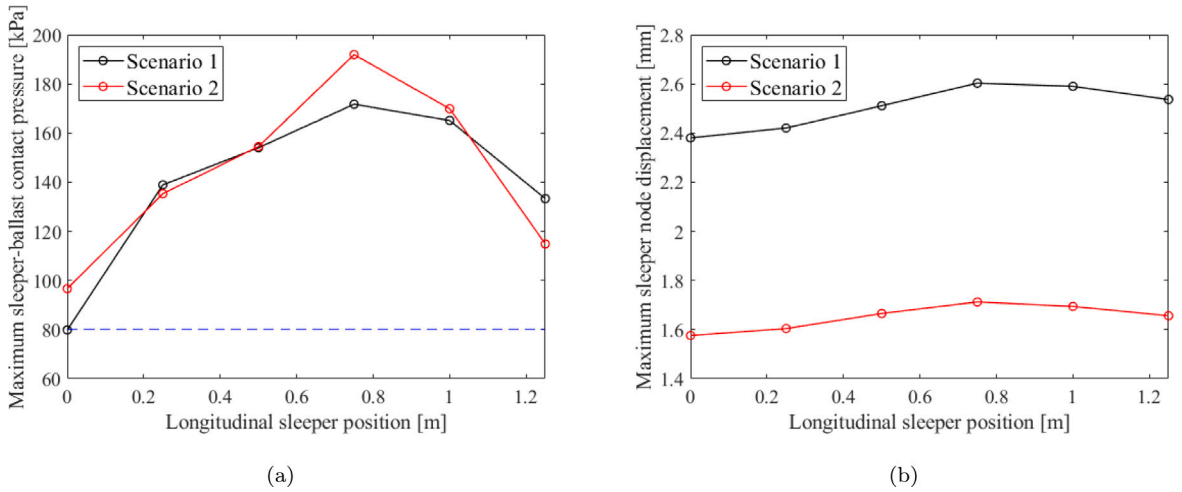

Fig. 10. Influence of two different transition zone designs on (a) maximum sleeper–ballast contact stress along sleeper 10 (with 6 vertical DOFs), and (b) corresponding maximum sleeper displacements.

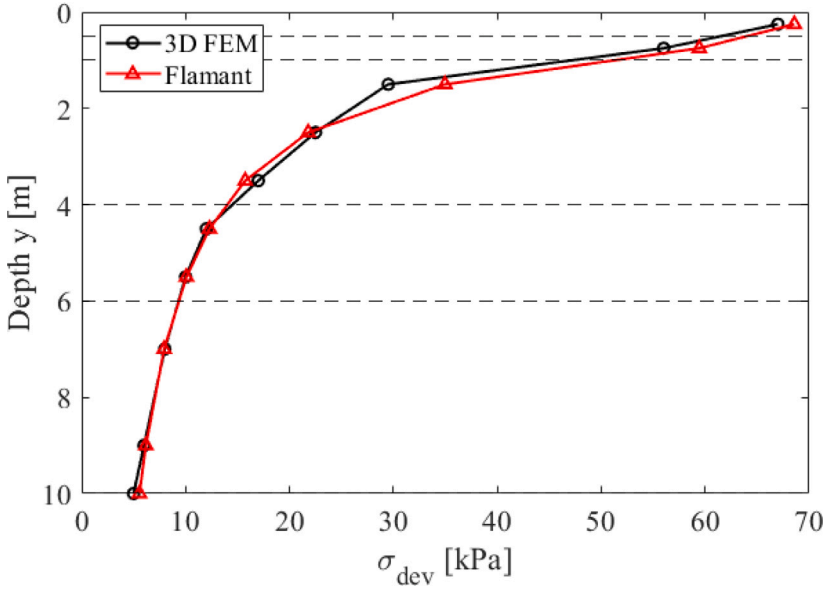

Fig. 11. Comparison of calculated deviatoric stress versus depth in layered subgrade using Flamant's solution and the 3D FE model. Single concentrated (static) load at the interface between the ballast layer and the layered subgrade, i.e. on the subgrade surface beneath sleeper 35. The interfaces between different layers are indicated by dashed black lines.

As a result, some sleepers located near the transition are subjected to greater accumulated settlement, which is reflected as a local dip in unloaded rail displacement in all corresponding figures.

In Scenario 3, the use of softer rail pads on the stiffer track form has a moderately positive effect in reducing differential settlement on the ballasted side, owing to the reduced stiffness gradient. It also has a beneficial impact on the loading conditions of the stiffer track form, although this is not shown here. The transition wedge reduces the settlement in the subgrade and lowers the local maximum in differential settlement adjacent to the transition. However, the additional stiffness gradient introduced by the wedge creates a new local maximum in differential settlement at its far end. When considering the case with traffic direction from the ballasted track to the slab track, the local maximum appears at sleeper 8, whereas for the opposite travel direction, the maximum occurs at sleeper 5. Additionally, the amplitude of the maximum settlement is slightly higher when traffic moves from the softer track form to the stiffer one.

The progressive development of track irregularities due to differential settlement and the formation of voided sleepers near the transition over one year of traffic is illustrated in Fig. 15. As voided sleepers gradually form in the vicinity of the transition, the vehicle load is redistributed to adjacent sleepers (with increasing sleeper numbers, as shown in Fig. 2), thereby shifting the location of the maximum settlement downstream relative to the transition. However, due to the hardening behaviour incorporated in the settlement models, where the threshold for further settlement increases with accumulated settlement, the process will ultimately reach a stabilisation. This manifests as a reduction in settlement rate over time.

Conclusions

A methodology for predicting long-term differential settlement in railway transition zones has been presented, combining time-domain simulations of vertical dynamic vehicle–track interaction with empirical formulations for the ballast and subgrade settlement. The simulation framework integrates a 2D vehicle model, a 3D nonlinear FE representation of the track superstructure, and a reduced-order 3D linear

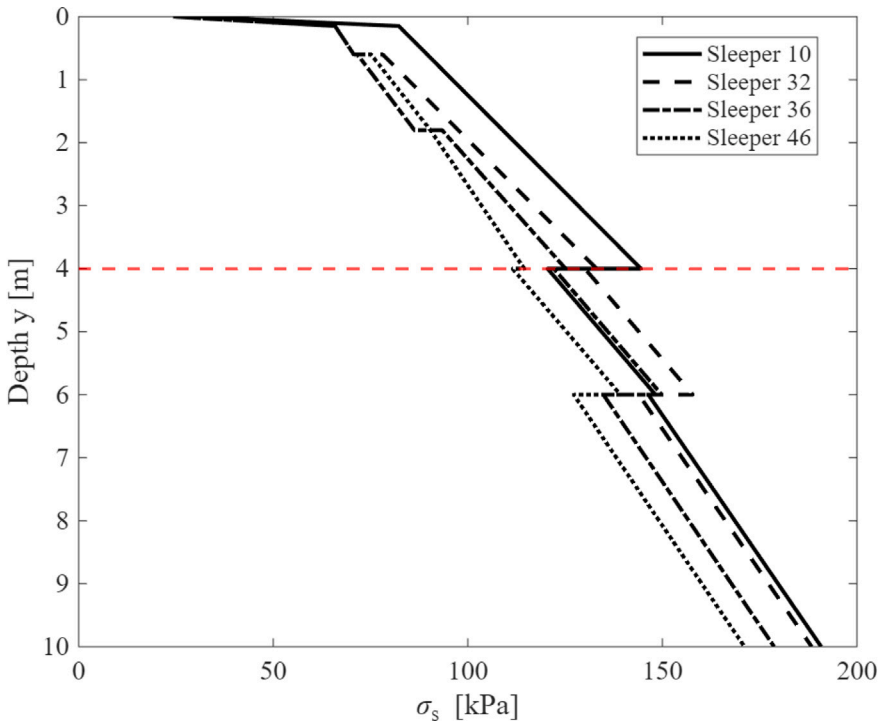

Fig. 12. Distribution of shear strength within the soil layers as a function of depth, evaluated using Eqs. (18)–(19). The bottom surface of the cubic wedge section is located 4 m below the interface between the ballast and the sub-ballast.

FE model of the stratified subgrade. This integrated approach captures the mechanical interaction between structural and geotechnical components, enabling the assessment of differential settlement, progressive sleeper voiding, redistribution of sleeper–ballast contact stresses, and the cumulative evolution of track geometry irregularities.

An iterative procedure is employed to capture the incremental settlement of the ballast and subgrade under a prescribed accumulated traffic load, reflecting the gradual deterioration of track geometry over time. The framework was applied to study a transition between a ballasted track on embankment and a slab track on a rigid engineering structure, and to investigate various design measures aimed at reducing the stiffness gradient and mitigating differential settlement within the transition zone. The findings indicate that both a transition wedge on the softer ballasted side and softer rail pads on the stiffer slab track side, when applied individually, are effective in reducing differential settlement. The analysis further highlights the distinct contributions of the ballast and the subgrade. In the short term, a softer subgrade accommodates lower sleeper–ballast contact pressures and ballast settlement, but leads to greater settlement within the subgrade due to the weaker soil conditions. Conversely, a stiffer subgrade increases the stresses at the sleeper–ballast interface, resulting in higher ballast degradation but reduced subgrade settlement. While the transition wedge reduces subgrade settlement within its extent, it may introduce a new local maximum in differential settlement at its downstream end if not properly designed, owing to the emergence of an additional stiffness gradient.

The investigation shows that differential settlement predominantly develops on the ballasted side of the transition, with local maxima forming between sleepers 5 and 10. The location of the maximum depends on traffic direction, occurring at sleeper 8 for traffic moving from ballasted track to slab track, but at sleeper 5 for the opposite direction, with the amplitude of the maximum being slightly higher in the former case. The use of softer rail pads provides a moderate reduction in differential settlement by lowering the stiffness gradient. Over time, settlement accumulation stabilises due to the hardening behaviour of the models, although this occurs only after significant degradation has developed within the transition zone.

It is recognised that soil behaviour may be nonlinear. However, within the present framework it is not possible to derive a ROM for a nonlinear system. Moreover, the ROM employed in this study is based on static condensation and therefore does not incorporate frequency-dependent dynamic effects. Furthermore, the settlement parameters employed in this study are site- and track-specific and would therefore need to be revised or recalibrated for other conditions on the basis of appropriate field measurements or dedicated site investigations. The current approach also neglects the influence of principal stress rotation on the track response, even though such rotation may influence the permanent deformation of geomaterials. These aspects may be addressed in future work.

CRediT authorship contribution statement

Kourosh Nasrollahi: Writing – original draft, Visualization, Validation, Software, Methodology, Investigation, Formal analysis, Data curation, Conceptualization. **Jens C.O. Nielsen:** Writing – review & editing, Supervision, Resources, Project administration, Methodology, Funding acquisition, Conceptualization. **Jelke Dijkstra:** Writing – review & editing, Supervision, Resources, Methodology, Funding acquisition, Conceptualization.

Declaration of competing interest

The authors declare that they have no known competing financial interests or personal relationships that could have appeared to influence the work reported in this paper.

Acknowledgements

The current study is part of the ongoing activities in CHARMEC, Chalmers Railway Mechanics (www.chalmers.se/charmec). Parts of the study have been funded by the Europe's Rail Flagship Project IAM4RAIL – Holistic, under grant agreement 101101966. Parts of the computations were enabled by resources provided by Chalmers e-Commons.

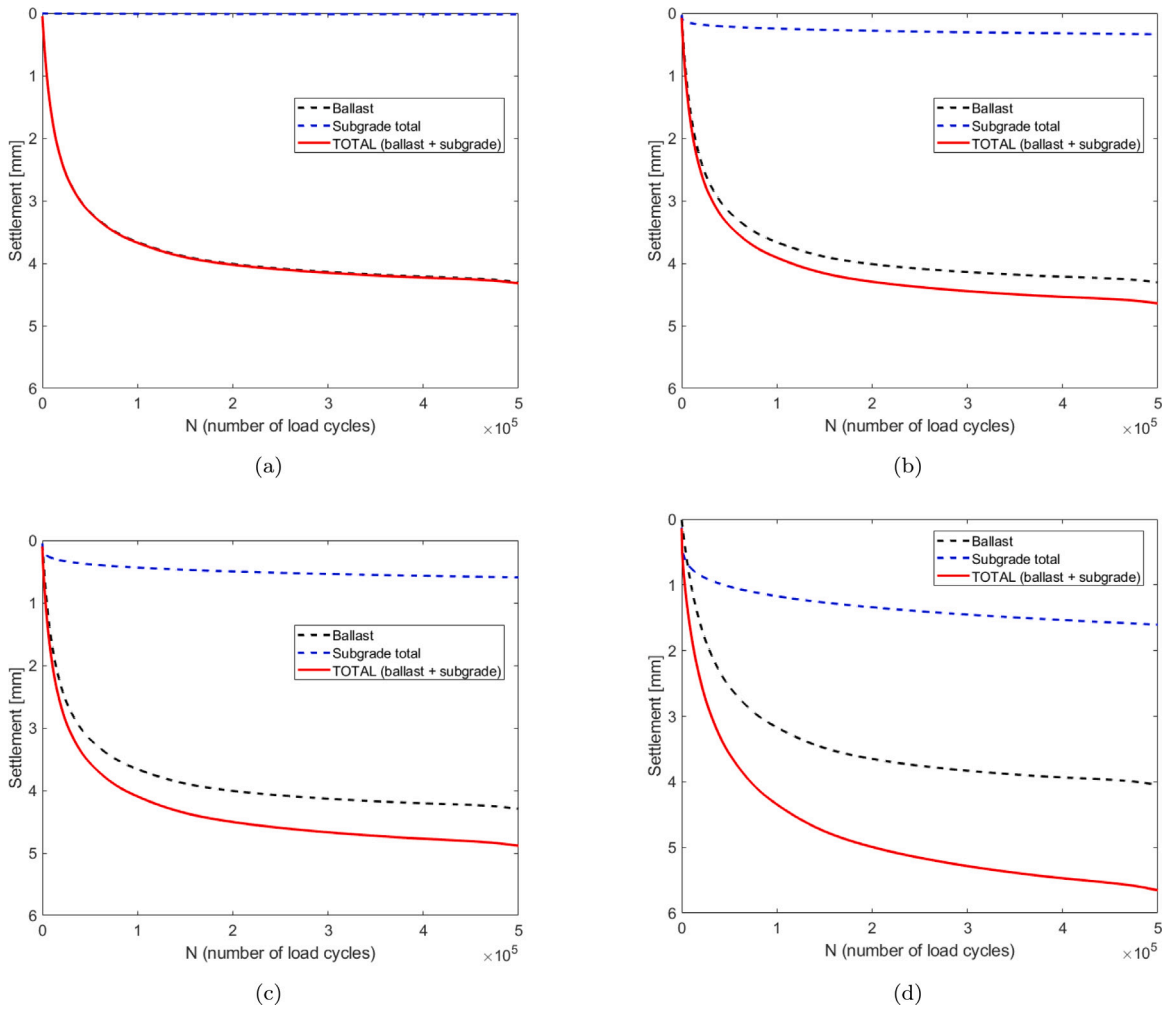

Fig. 13. Calculated contributions to the long-term settlement of the ballast and subgrade layers using the threshold visco-plastic approach and the Li and Selig model. Results are shown for four sleepers on the ballasted side of a transition between ballasted track and slab track on a bridge, with a transition wedge (Scenario 2) extending from sleeper 1 to 32 (numbered from the transition): (a) sleeper 10, (b) sleeper 32, (c) sleeper 36, and (d) sleeper 46.

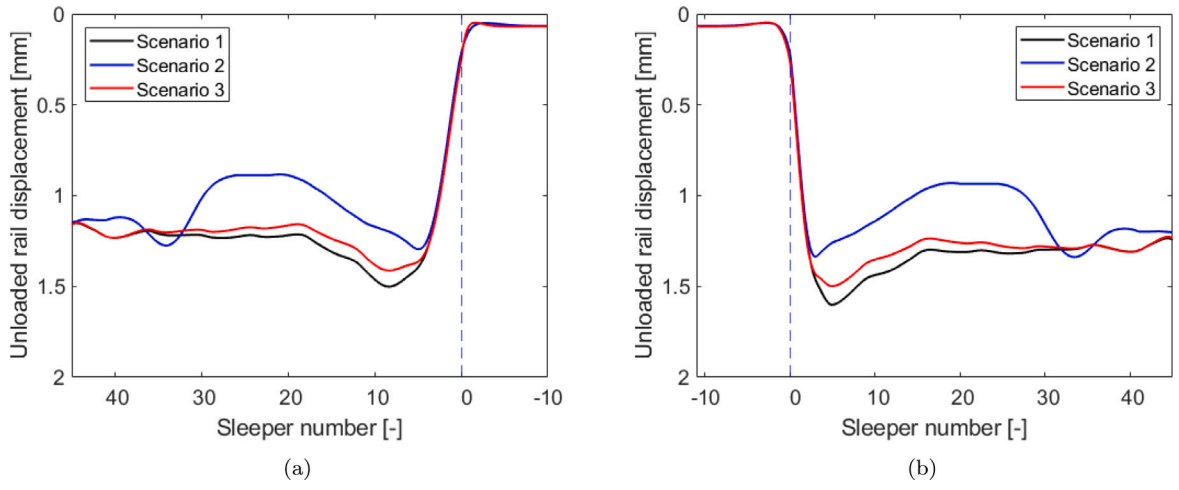

Fig. 14. Rail displacement due to gravity load and differential settlement after an accumulated traffic load of 15 MGT for two traffic directions: (a) ballasted track to slab track, and (b) slab track to ballasted track.

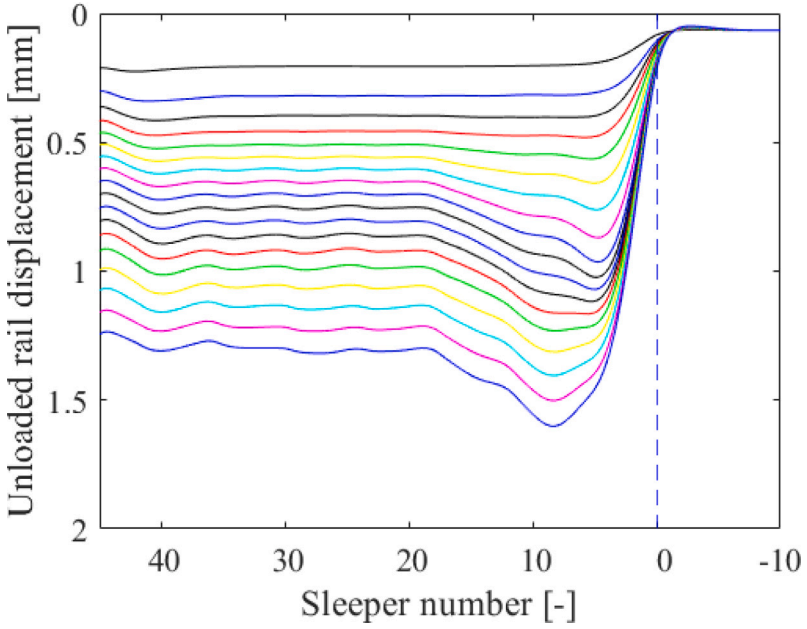

Fig. 15. Evolution of rail displacement due to gravity load and differential settlement, shown for iterations 1 through 18. Scenario 1 with traffic direction from the ballasted track to the slab track.

Data availability

Data will be made available on request.

References

[1] Varandas J, Hölscher P, Silva M. Settlement of ballasted track under traffic loading: Application to transition zones. Proc Inst Mech Eng Part F: J Rail Rapid Transit 2014;228:242–59.

[2] Shahraki M, Warnakulasooriya C, Witt KJ. Numerical study of transition zone between ballasted and ballastless railway track. Transp Geotech 2015;3:58–67.

[3] Indraratna B, Sajjad MB, Ngo T, Correia AG, Kelly R. Improved performance of ballasted tracks at transition zones: A review of experimental and modelling approaches. Transp Geotech 2019;21:100260.

[4] Aggestam E, Nielsen JCO. Multi-objective optimisation of transition zones between slab track and ballasted track using a genetic algorithm. J Sound Vib 2019;446:91–112.

[5] Nasrollahi K, Nielsen JCO, Aggestam E, Dijkstra J, Ekh M. Prediction of long-term differential track settlement in a transition zone using an iterative approach. Eng Struct 2023;283.

[6] Nasrollahi K, Ramos A, Nielsen JCO, Dijkstra J, Ekh M. Benchmark of calibrated 2D and 3D track models for simulation of differential settlement in a transition zone using field measurement data. Eng Struct 2024;316:118555.

[7] Jain A, Metrikine AV, Steenbergen M, Dalen Kv. Railway transition zones: Energy evaluation of a novel transition structure for critical loading conditions. J Vib Eng Technol 2025;13(1):15.

[8] Ahmadi A, Nasrollahi K, Nielsen JCO, Dijkstra J. Dynamic vehicle–track interaction and differential settlement in a transition zone on railway ballast—An integrated 3D discrete–continuum model. Comput Geotech 2026;190:107737.

[9] Nasrollahi K, Dijkstra J, Nielsen J. Towards real-time condition monitoring of a transition zone in a railway structure using fibre bragg grating sensors. Transp Geotech 2024;44:101166.

[10] Ramos A, Correia AG, Nasrollahi K, Nielsen JCO, Calçada R. Machine learning models for predicting permanent deformation in railway tracks. Transp Geotech 2024;47:101289.

[11] Nasrollahi K, Nielsen J. Influence of sleeper base area and spacing on long-term differential settlement in a railway track transition zone. In: Proceedings of the sixth international conference on railway technology: research, development and maintenance. Prague, Czech Republic; 2024.

[12] Soundararajan S, Raychowdhury P, Nimbalkar S, et al. Field investigation of dynamic response of elevated ballasted track focusing on transition zone. Transp Infrastruct Geotechnol 2026;13:20.

[13] Sañudo R, dell'Olio L, Casado J, Carrascal I, Diego S. Track transitions in railways: A review. Constr Build Mater 2016;112:140–57.

[14] Wang H, Markine V. Corrective countermeasure for track transition zones in railways: Adjustable fastener. Eng Struct 2018;169:1–14.

[15] Nasrollahi K. Transition zone design for reduced track settlements – field measurements and numerical simulations [Ph.D. thesis], Gothenburg, Sweden: Chalmers University of Technology; 2025.

[16] Knothe K, Grassie SL. Modelling of rail vehicle/track interaction at high frequencies. Veh Syst Dyn 1993;22(3–4):209–62.

[17] Shih J, Thompson D, Zervos A. The effect of boundary conditions, model size and damping models in the finite element modelling of a moving load on a track/ground system. Soil Dyn Earthq Eng 2016;89:12–27.

[18] Ramos A, Gomes Correia A, Calçada R, Connolly DP. Ballastless railway track transition zones: An embankment to tunnel analysis. Transp Geotech 2022;33:100728.

[19] Baeza L, Roda A, Nielsen J. Railway vehicle/track interaction analysis using a modal substructuring approach. J Sound Vib 2006;293(1):112–24.

[20] Battiato G, Firrone CM, Berruti TM, Epureanu BI. Reduction and coupling of substructures via Gram–Schmidt Interface modes. Comput Methods Appl Mech Engrg 2018;336:187–212.

[21] Craig RR, Bampton MC. Coupling of substructures for dynamic analyses. AIAA J 1968;6(7):1313–9.

[22] Vilhelmson H, Pålsson BA, Nielsen JCO, Ossberger U, Sehner M, Loy H. Dynamic vehicle–track interaction and structural loading in a crossing panel–calibration and assessment of a model with a 3D representation of the crossing rai. Veh Syst Dyn 2024;62(12):3168–90.

[23] Gräbe P, Clayton C, Shaw F. Deformation measurement on a heavy haul track formation. In: Proceedings of the 8th international heavy haul conference. Rio de Janeiro, Brazil: International Heavy Haul Association; 2005.

[24] Kaynia AM, Madshus C, Zackrisson P. Ground vibration from high-speed trains: Prediction and countermeasure. J Geotech Geoenvironmental Eng 2000;126(6):531–7.

[25] Li X, Nielsen JCO, Pålsson BA. Simulation of track settlement in railway turnouts. Veh Syst Dyn 2014;52(sup1):421–39.

[26] Suiker ASJ. The mechanical behaviour of ballasted railway tracks [Ph.D. thesis], Delft, The Netherlands: Delft University of Technology; 2002.

[27] Punetha P, Nimbalkar S, Khabbaz H. Analytical evaluation of ballasted track substructure response under repeated train loads. Int J Geomech 2020;20(7):04020093.

[28] Peltomäki M, Kolisoja P, Luomala H. Novel permanent deformation model for granular materials. Transp Geotech 2025;51:101494.

[29] Li D, Selig ET. Cumulative plastic deformation for fine-grained subgrade soils. J Geotech Eng 1996;122(12):1006–13.

[30] Abadi T, Le Pen L, Zervos A, Powrie W. A review and evaluation of ballast settlement models using results from the Southampton Railway Testing Facility (SRTF). Procedia Eng 2016;143:999–1006.

[31] Verruijt A. In: An introduction to soil dynamics, vol. 24, Springer Science & Business Media; 2009.

[32] Nielsen JCO. High-frequency vertical wheel–rail contact forces—Validation of a prediction model by field testing. Wear 2008;265(9–10):1465–71.

[33] Nielsen JCO. Dynamic interaction between wheel and track – a parametric search towards an optimal design of rail structures. Veh Syst Dyn 1994;23(1):115–32.

[34] Zhai W, Xia H, Cai C, Gao M, Li X, Guo X, Zhang N, Wang K. High-speed train–track–bridge dynamic interactions – Part I: Theoretical model and numerical simulation. Int J Rail Transp 2013;1(1–2):3–24.
[35] Wolf JP, Deeks AJ. Foundation vibration analysis: A strength-of-materials approach. Elsevier 2004;42(01):218.
[36] Gazetas G. Foundation vibrations. In: Foundation engineering handbook. New York: Van Nostrand Reinhold; 1991, p. 553–93.
[37] Milne D, Le Pen L, Thompson D, Powrie W. Properties of train load frequencies and their applications. J Sound Vib 2017;397:123–40.
[38] Craig RRJ, Chang CJ. Substructure coupling for dynamic analysis and testing. Tech. rep., National Aeronautics and Space Administration; 1977.
[39] Powrie W, Yang LA, Clayton CRI. Stress changes in the ground below ballasted railway track during train passage. Proc Inst Mech Eng Part F: J Rail Rapid Transit 2007;221(2):247–62.
[40] Charoenwong C, Connolly DP, Woodward PK, Galvín P, Alves Costa P. Analytical forecasting of long-term railway track settlement. Comput Geotech 2022;143:104601.
[41] Peng B, Van Dalen KN, Li Z, Kaewenruen S, Xu L, Shiau J, Lu T. Spatial-temporal evolution prediction of train-induced settlement in railway transition zone using a simplified iterative framework. J Sound Vib 2025;119360.
[42] Nielsen JCO, Li X. Railway track geometry degradation due to differential settlement of ballast/subgrade – numerical prediction by an iterative procedure. J Sound Vib 2018;412:441–56.
[43] Oscarsson J, Dahlberg T. Dynamic train-track-ballast interaction-computer models and full-scale experiments. Veh Syst Dyn 1998;29(S1):73–84.
[44] Zhai W, Sun X. A detailed model for investigating vertical interaction between railway vehicle and track. Vehicle SYst. Dynamics 1994;23(S1):603–15.
[45] Guo Y, Zhai W. Long-term prediction of track geometry degradation in high-speed vehicle–ballastless track system due to differential subgrade settlement. Soil Dyn Earthq Eng 2018;113:1–11.